Time-Dependent Eddy-Mean Energy Diagrams and Their Application to the Ocean

RU CHEN

Scripps Institution of Oceanography, University of California, San Diego, La Jolla, California

ANDREW F. THOMPSON

California Institute of Technology, Pasadena, California

GLENN R. FLIERL

Massachusetts Institute of Technology, Cambridge, Massachusetts

(Manuscript received 5 January 2016, in final form 7 July 2016)

ABSTRACT

Insight into the global ocean energy cycle and its relationship to climate variability can be gained by examining the temporal variability of eddy–mean flow interactions. A time-dependent version of the Lorenz energy diagram is formulated and applied to energetic ocean regions from a global, eddying state estimate. The total energy in each snapshot is partitioned into three components: energy in the mean flow, energy in eddies, and energy temporal anomaly residual, whose time mean is zero. These three terms represent, respectively, correlations between mean quantities, correlations between eddy quantities, and eddy-mean correlations. Eddy–mean flow interactions involve energy exchange among these three components. The temporal coherence about energy exchange during eddy–mean flow interactions is assessed. In the Kuroshio and Gulf Stream Extension regions, a suppression relation is manifested by a reduction in the baroclinic energy pathway to the eddy kinetic energy (EKE) reservoir following a strengthening of the barotropic energy pathway to EKE; the baroclinic pathway strengthens when the barotropic pathway weakens. In the subtropical gyre and Southern Ocean, a delay in energy transfer between different reservoirs occurs during baroclinic instability. The delay mechanism is identified using a quasigeostrophic, two-layer model; part of the potential energy in large-scale eddies, gained from the mean flow, cascades to smaller scales through eddy stirring before converting to EKE. The delay time is related to this forward cascade and scales linearly with the eddy turnover time. The relation between temporal variations in wind power input and eddy–mean flow interactions is also assessed.

1. Introduction

Evaluating ocean energetics not only improves our fundamental understanding of the ocean but also is a useful step to construct general circulation models with energetics consistent with the ocean (e.g., Eden et al. 2014). Therefore, the source, sink, and transformation of energy in the global ocean has received much attention (e.g., Wunsch and Ferrari 2004; Ferrari and Wunsch 2009; Zemskova et al. 2015). Many studies exist about energetics during eddy–mean flow interactions, and most of these focus on characterizing the spatial structures and magnitude of energy conversion rates between the mean and eddies from a long-term, time-mean perspective (e.g., von Storch et al. 2012; Liang et al. 2012; Chen et al. 2014a; Kang and Curchitser 2015). Efforts in diagnosing the energy cascade diagram in the frequency–wavenumber domain, as summarized by Ferrari and Wunsch (2009), also mainly focus on a long-term, time-mean perspective (e.g., Scott and Wang 2005; Scott and Arbic 2007; Arbic et al. 2012).

Though it has received less attention, the temporal variability of the energy cycle is an important topic for the following two reasons: First, ocean motions are turbulent with temporal variability ranging from superinertial

Corresponding author address: Ru Chen, Scripps Institution of Oceanography, University of California, San Diego, 9500 Gilman Dr., Mail Code 0230, La Jolla, CA 92093-0230.
E-mail: ruchen@alum.mit.edu

DOI: 10.1175/JPO-D-16-0012.1

to centennial scales (e.g., Ferrari and Wunsch 2009). Depicting the temporal variability of energetics itself is an integral perspective of evaluating the oceanic temporal variability. Second, eddy kinetic energy (EKE) is a dominant part of total kinetic energy (e.g., von Storch et al. 2012), and strong temporal variability of EKE on seasonal and/or interannual time scales has been identified in many regions, such as the Southern Ocean, Kuroshio Extension, and the South Pacific (e.g., Qiu and Chen 2004, 2010; Hogg et al. 2015). Since EKE largely controls the magnitude of eddy mixing rates (e.g., Killworth 1997; Chen et al. 2014b, 2015), to which the meridional overturning circulation and climate model results are sensitive (e.g., Gregory 2000; Spence et al. 2009; Gnanadesikan et al. 2015), evaluating the temporal EKE variability is important.

Considering that eddy–mean flow interactions greatly control the eddy energy budget (e.g., Wunsch 1998; Stammer and Wunsch 1999; von Storch et al. 2012), one way to evaluate the EKE variability is to assess the temporal variability of these interactions. Therefore, this study introduces a time-dependent energy diagram for eddy–mean flow interactions (section 2). The classic Lorenz energy cycle, introduced by Lorenz (1955) and successfully applied to previous energy studies (e.g., von Storch et al. 2012), depicts the local eddy–mean flow interactions from a time-mean (or zonal mean) energy perspective. Chen et al. (2014a) extended the Lorenz energy diagram to the nonlocal regime from a time-mean perspective and introduced the concept of local/nonlocal eddy–mean flow interactions. If the amount of energy released by the mean flow is not equal to the amount of energy received by eddies, eddy–mean flow interactions are nonlocal. On the other hand, if these two quantities are equal, eddy–mean flow interactions are local. This study further extends the nonlocal, eddy-mean energy diagram from Chen et al. (2014a) to the time-dependent scenario.

Besides evaluating the EKE variability, the time-dependent energy diagram is also useful in tracking the pathway of wind power input in the energy system. In contrast to the atmosphere acting as a heat engine (Oort and Peixóto 1983), the ocean is largely wind driven: the total power input into the ocean is 6.6 TW, of which 4.1 TW is wind power input (von Storch et al. 2012). The wind power input undergoes significant temporal variability (Huang et al. 2006), and not surprisingly, EKE levels show a sensitivity to this wind variability. For example, in regions with substantial wind energy, eddy variability is well correlated with the wind forcing magnitude on annual and interannual time scales (Stammer and Wunsch 1999). In the Southern Ocean, the EKE maximum lags the wind stress maxima by 2–3 yr (Meredith and Hogg 2006); the regional EKE, however, has a complex relation with wind stress (Thompson and Naveira-Garabato 2014). Oceanic variability can also be driven by intrinsic nonlinearity (e.g., Arbic et al. 2014). It remains largely unclear to what degree eddy–mean flow interactions energetics covary with the wind power input. Their relations are depicted in section 3c; compared to the Southern Ocean and western boundary extension regions, the subtropical gyre area, which has more linear characteristics, has a greater coherence between the wind power input and eddy–mean flow interactions.

Our goals are twofold: 1) to introduce a time-dependent energy diagram for eddy–mean flow interactions (section 2) and 2) to depict the temporal variability of eddy–mean flow interactions energetics in energetic regions from a frequency perspective (section 4). Section 3 introduces the setup of the main model used for the energy diagnosis: the Estimating the Circulation and Climate of the Ocean, phase 2, high-resolution global ocean and sea ice data synthesis (ECCO2) state estimate (e.g., Menemenlis et al. 2008; Chen et al. 2014a). Section 4 examines the coupling between energy transfer terms composing eddy–mean flow interactions; the "delay phenomenon" and "suppression phenomenon" are identified. The origin for the delay phenomenon is discussed using a quasigeostrophic (QG) two-layer model. Section 5 is the conclusion.

2. Formulation of the time-dependent energy diagram

a. *Decomposition of kinetic energy reservoir and available potential energy reservoir*

As in Chen et al. (2014a), we define the mean flow as the temporal average over the entire available record (1992–2007 in the ECCO2 state estimate) and define eddies as the deviation from the mean. The derivations in Chen et al. (2014a) are essentially the same as Murakami (2011) and Murakami et al. (2011), who applied this type of split in the energy equations to atmospheric problems.[1] We continue to use the Chen et al. (2014a) notation about energy reservoirs for convenience in this study of ocean energetics.

A first step to formulate the time-dependent energy diagram is to decompose the energy reservoirs at each snapshot. The total kinetic energy of the full flow field is defined as

[1] We have just become aware of these excellent papers and the way our previous paper independently followed very similar paths. This paper, however, extends the argument into the time domain.

$$K_T(x,y,z,t) = \frac{1}{2}\rho_0(u^2+v^2) = K_M(x,y,z) + K_E(x,y,z,t) + K_R(x,y,z,t), \quad (1)$$

where u and v are zonal and meridional velocities, respectively, and ρ_0 is the constant reference density, which is 1027.5 kg m^{-3} in the ECCO2 model. Here, K_M denotes the kinetic energy in the mean flow,

$$K_M(x,y,z) = \frac{1}{2}\rho_0(\overline{u}^2+\overline{v}^2), \quad (2)$$

and $K_E(x,y,z,t)$ denotes the kinetic energy in eddies (EKE),

$$K_E(x,y,z,t) = \frac{1}{2}\rho_0(u'^2+v'^2), \quad (3)$$

where $\overline{\cdot}$ is the time mean, and $\cdot'$ denotes the deviation from time mean. The kinetic energy anomaly residual is thus

$$K_R(x,y,z,t) = \rho_0(u'\overline{u}+v'\overline{v}). \quad (4)$$

We chose a widely used QG definition of available potential energy (APE; e.g., Pedlosky 1987; Oort et al. 1989, 1994; Huang 2010; Brown and Fedorov 2010). The total APE of the full flow field P_T is

$$P_T(x,y,z,t) = -\frac{g}{2n_0}[\rho^*(x,y,z,t)]^2. \quad (5)$$

As stated in Chen et al. (2014a), n_0 denotes the vertical gradient of the local potential density averaged over time and the entire globe at a given depth, that is,

$$n_0(z) = -\frac{\rho_0}{g}N^2(z) = \left\langle \left[\frac{\partial\rho(x,y,z,t)}{\partial z}\right]_{x,y,t} \right\rangle - \left\langle \left[\frac{\partial\rho(S,\theta,z)}{\partial z}\right]_{S,\theta} \right\rangle, \quad (6)$$

where $\langle\cdot\rangle$ represents the global average at a selected depth level, $N^2(z)$ is the temporally and globally averaged buoyancy frequency (Huang 2010), and S and θ represent salinity and potential temperature at time t and position (x, y, z). Here, $\rho^*(x, y, z, t) = \rho(x, y, z, t) - \langle\overline{\rho(x, y, z, t)}\rangle$. The terms $\rho(x, y, z, t)$, $\overline{\rho(x, y, z, t)}$, and $\langle\overline{\rho(x, y, z, t)}\rangle$ are, respectively, the in situ density in the instantaneous state, the time-mean state, and the reference state.

Similar to kinetic energy, the total APE is decomposed into three parts:

$$P_T(x,y,z,t) = -\frac{g}{2n_0(z)}[\rho^*(x,y,z,t)]^2 = P_M(x,y,z) + P_E(x,y,z,t) + P_R(x,y,z,t). \quad (7)$$

Here, P_M is the mean available potential energy, that is, the APE stored in the time-mean state:

$$P_M(x,y,z) = -\frac{g}{2n_0(z)}\overline{\rho^*(x,y,z,t)}^2. \quad (8)$$

The term P_E denotes eddy available potential energy (EAPE), that is, the APE stored in eddies:

$$P_E(x,y,z) = -\frac{g}{2n_0(z)}[\rho'(x,y,z,t)]^2. \quad (9)$$

Note that $(\rho^*)' = \rho'$. The APE anomaly residual is

$$P_R(x,y,z,t) = -\frac{g}{2n_0(z)}[2\overline{\rho^*(x,y,z,t)}\rho'(x,y,z,t)]. \quad (10)$$

The total potential energy includes APE and background potential energy, but the energy exchange between potential energy and kinetic energy reservoirs only occurs between APE and kinetic energy (Winters et al. 1995). Although the QG definition of APE is an approximate definition of APE, the energy exchange between the QG APE and kinetic energy is exactly the same as the energy exchange between the exact total potential energy and kinetic energy. Therefore, the QG definition of APE only affects the estimation of the APE magnitude and the energy transfer rates among P_M, P_E, and P_R.

b. Energy equations

The governing equations for energy reservoirs described in section 2a are

$$\frac{\partial}{\partial t}K_M + \frac{\partial}{\partial x_j}(u_jK_M + \overline{u}_j\overline{p^*}) = E_{P_M\to K_M} + E_{K_R\to K_M} + X_{K_M}, \quad (11)$$

$$\frac{\partial}{\partial t}K_E + \frac{\partial}{\partial x_j}(u_jK_E + u_j'p') = E_{P_E\to K_E} + E_{K_R\to K_E} + X_{K_E}, \quad (12)$$

$$\frac{\partial}{\partial t}K_R + \frac{\partial}{\partial x_j}(u_jK_R + \overline{u}_jp' + u_j'\overline{p^*}) = E_{P_R\to K_R} - (E_{K_R\to K_E} + E_{K_R\to K_M}) + X_{K_R}, \quad (13)$$

$$\frac{\partial}{\partial t}P_M + \frac{\partial}{\partial x_j}(u_jP_M) = E_{P_R\to P_M} - E_{P_M\to K_M} + X_{P_M} + R_{P_M}, \quad (14)$$

$$\frac{\partial}{\partial t}P_E + \frac{\partial}{\partial x_j}(u_jP_E) = E_{P_R\to P_E} - E_{P_E\to K_E} + X_{P_E} + R_{P_E}, \quad \text{and} \quad (15)$$

TABLE 1. Terms about eddy–mean flow interactions from the time-dependent energy diagnostic framework in section 2b. Here, $i = 1$ and 2, denoting zonal and meridional directions, and $j = 1$, 2, and 3, denoting zonal, meridional and vertical directions.

Term	Mathematical form	Meaning
$E_{P_E \to K_E}$	$-g\rho' w'$	Eddy transfer rate from P_E to K_E through vertical eddy density fluxes.
$E_{P_R \to K_R}$	$-g(\overline{\rho^*}\overline{w'} + \rho'\overline{w})$	Eddy transfer rate from P_R to K_R through vertical density fluxes.
$E_{K_R \to K_M}$	$\frac{\partial}{\partial x_j}(u_j' K_M) - \rho_0 \overline{u}_i \frac{\partial}{\partial x_j}\overline{u_j' u_i'}$	Eddy transfer rate from K_R to K_M through momentum fluxes.
$E_{K_R \to K_E}$	$-\rho_0 u_i' u_j' \frac{\partial}{\partial x_j}\overline{u}_i + \rho_0 u_i' \frac{\partial}{\partial x_j}\overline{u_i' u_j'}$	Eddy transfer rate from K_R to K_E through momentum fluxes.
$E_{P_R \to P_M}$	$\frac{g}{n_0}\overline{\rho^*}\frac{\partial}{\partial x_i}(\overline{u_i'\rho'}) + \frac{\partial}{\partial x_i}(u_i' P_M)$	Eddy transfer rate from P_R to P_M through density fluxes.
$E_{P_R \to P_E}$	$\frac{g}{n_0}\rho' u_i' \frac{\partial}{\partial x_i}\overline{\rho^*} - \frac{g}{n_0}\rho' \frac{\partial}{\partial x_i}(\overline{u_i'\rho'})$	Eddy transfer rate from P_R to P_E through density fluxes.

$$\frac{\partial}{\partial t}P_R + \frac{\partial}{\partial x_j}(u_j P_R) = -(E_{P_R \to P_M} + E_{P_R \to P_E}) - E_{P_R \to K_R} + X_{P_R} + R_{P_R}, \tag{16}$$

where u_j is the three-dimensional velocity vector, p is hydrostatic pressure, and $\cdot^*$ denotes the deviation of a variable from its global horizontal and time mean at each depth level. Note that we derived the above governing equations by writing the instantaneous advection of the energy reservoirs by total velocity and using the momentum equations to figure out what other terms are. Derivation details, including the rationale of including the advection of total flow in each energy equation, are provided in appendix A.

The $E_{a \to b}$ terms on the right-hand side of Eqs. (11)–(16) denote the energy transfer rate from the reservoir a to reservoir b. These $E_{a \to b}$ terms, except $E_{P_M \to K_M}$, are terms about eddy–mean flow interactions, which are the focus of this study (Table 1). The temporal variability of each kinetic energy component is balanced by advection, pressure work, E terms and X terms (which denote the energy change rate due to horizontal and vertical friction, wind power input, and bottom drag) [Eqs. (11)–(13)]. The temporal change rate of each APE component is balanced by the advection terms, E terms, R terms, and X terms, which represent the contribution of vertical mixing, heat, and freshwater fluxes to the APE budgets [Eqs. (14)–(16)]. The R terms in the APE budgets, absent in the quasigeostrophic framework, have higher-order Rossby numbers (Chen et al. 2014a).

c. *A time-dependent energy diagram for eddy–mean flow interactions and its comparison with previous literature*

Equations (11)–(16) can be represented symbolically on a diagram like Fig. 1a. Blue and red arrows in Fig. 1a refer to eddy–mean flow interactions terms associated with eddy momentum and density fluxes, respectively. This diagram, though simple, is to our knowledge, the first published time-dependent energy diagram for eddy–mean flow interactions. Previous studies mostly evaluate the time-mean, eddy–mean flow interactions energetics, with a focus on the EKE budget (e.g., Biastoch and Krauss 1999; Marchesiello et al. 2003; Mata et al. 2006; Liang et al. 2012). This diagram reveals that during eddy–mean flow interactions, the energy exchange actually occurs between K_M and K_R, K_R and K_E, P_R and P_R, and P_R and P_E. That is, eddy and mean energy reservoirs are not directly interacting with each other; they are directly interacting with K_R and P_R (rationale is available in the last paragraph of appendix A, section a. Generally, the energy exchange between K_M and K_R is not necessarily equal to the energy exchange between K_R and K_E, and the imbalances are compensated by advection of K_R, pressure work, and so on [Eq. (13)]. Similarly, the energy exchange between P_M and P_R is not necessarily equal to the energy exchange between P_R and P_E [Eq. (16)].

As stated in section 1, the time-dependent energy diagram (Fig. 1a) is an extension of the classic Lorenz energy diagram from Lorenz (1955) to the time-dependent and nonlocal regime. Compared to the classic Lorenz energy diagram, Fig. 1a includes two additional energy components (K_R and P_R). The existence of K_R and P_R is due to the lack of scale separation between zero-frequency (i.e., time mean) motions and motions at other frequencies. Though the time means of K_R and P_R are zero, their amplitudes can be nonnegligible in the total energy reservoir at any individual point in time (section 3b). Therefore, K_R and P_R contribute significantly to the temporal variability of total kinetic and potential energy.

The time-mean version of Figs. 1a and 1b is essentially the same as the eddy–mean flow interactions diagram from Chen et al. (2014a, their Fig. 1a). Chen et al. (2014a) introduced the concept of local and nonlocal eddy–mean flow interactions. If both $\overline{E_{K_R \to K_E} + E_{K_R \to K_M}}$ and $\overline{E_{P_R \to P_M} + E_{P_R \to P_E}}$ are zero, eddy–mean flow

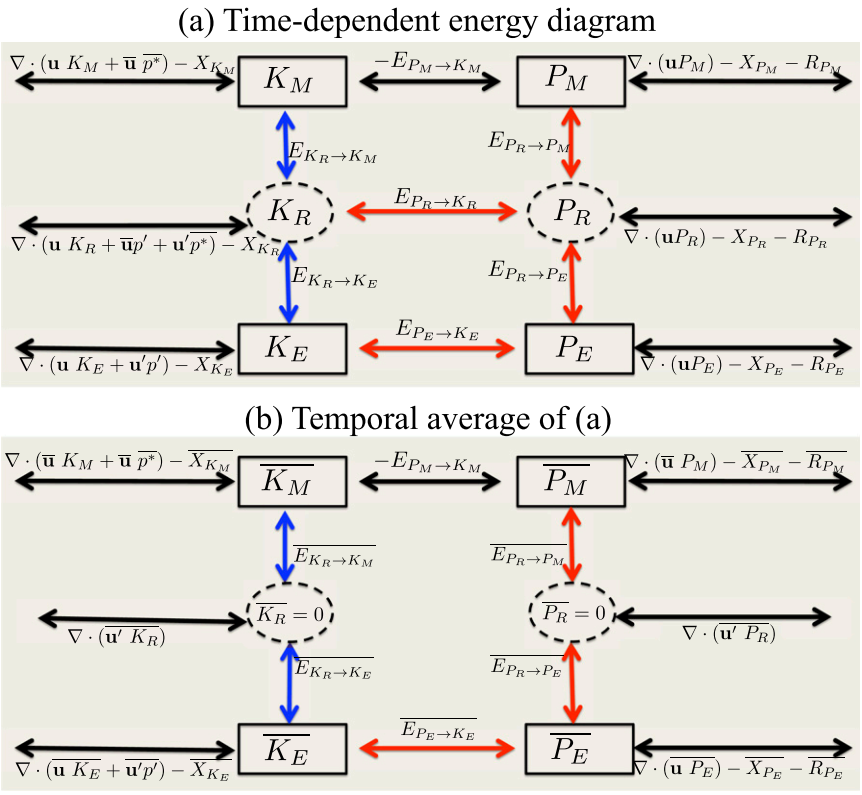

FIG. 1. Schematics illustrating the energy transfer through eddy–mean flow interactions. Blue arrows denote eddy–mean flow interactions terms associated with eddy momentum fluxes, and red arrows are those associated with eddy density fluxes. Black arrows represent other elements in the energy budgets [Eqs. (11)–(16)]. Arrows have two heads, as energy can transfer in either direction. (a) The time-dependent case [Eqs. (11)–(16)]. During eddy–mean flow interactions, as illustrated by red and blue arrows, energy does not transfer directly between the mean energy reservoir (K_M and P_M) and eddy energy reservoir (K_E and P_E); instead, energy is transferred between mean/eddy energy and the energy anomaly residual (K_R and P_R). The energy exchange between K_M and K_R is not necessarily equal to the energy exchange between K_R and K_E [Eq. (13)]. Similarly, the energy exchange between P_M and P_R is not necessarily equal to the energy exchange between P_R and P_E [Eq. (16)]. (b) The time-mean version of (a), which is essentially the same as Fig. 1 from Chen et al. (2014a).

interactions are local; otherwise, interactions are nonlocal. As discussed in detail in appendix A, section c, compared to Chen et al. (2014a), we provide additional insights about the time-mean, eddy-mean energy diagram: 1) The black dots shown in Fig. 1a in Chen et al. (2014a) are K_R and P_R, and 2) from a time-mean perspective, in the K_R and P_R budgets, eddy–mean flow interactions terms, indicated by the red and blue arrows, are balanced by the eddy advection of K_R and P_R:

$$\frac{\partial}{\partial x_j}(\overline{u_j' K_R}) = -(\overline{E_{K_R\to K_E} + E_{K_R\to K_M}}) \quad \text{and}$$

$$\frac{\partial}{\partial x_i}(\overline{u_i' P_R}) = -(\overline{E_{P_R\to P_M} + E_{P_R\to P_E}}), \tag{17}$$

where $\partial/\partial x_j$ and $\partial/\partial x_i$ are, respectively, three-dimensional and horizontal gradient operators.

3. ECCO2 model and basic depiction about energetics

a. *Tool: ECCO2 state estimate*

The time-dependent energy diagram in Fig. 1a is a direct extension of the diagram in Chen et al. (2014a). Therefore, we follow Chen et al. (2014a) and use the cube 87 version of the ECCO2 state estimate for the energy diagnosis. Some other recent studies (e.g., Zemskova et al. 2015) also indicate that the ECCO2 state estimate is suitable for evaluating ocean energetics. Details of the model configuration and fidelity are available in Chen et al. (2014a). The ECCO2 state estimate is dynamically consistent and suitable for budget diagnosis, as it is a free-forward model run using optimum values for uncertain parameters (e.g., forcing and

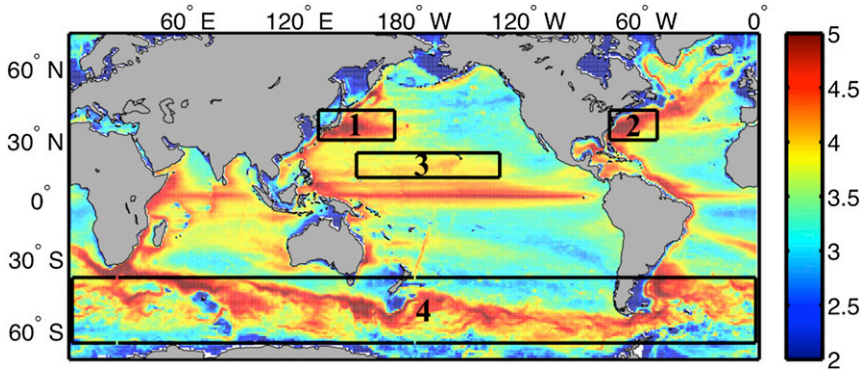

FIG. 2. The temporal average of the vertically integrated K_T (J m^{-2}) on a logarithmic scale. This study focuses on the four energetic regions, indicated by the black boxes: 1) the Kuroshio Extension, 2) Gulf Stream Extension, 3) a representative Pacific patch of the subtropical gyre, and 4) the Southern Ocean.

viscosity). These optimum values are determined by comparing observations with results from a set of sensitivity experiments, using the Green function approach (Menemenlis et al. 2008). In other words, the ECCO2 state estimate is constrained by observations, yet it is still dynamically consistent. The model, with a mean horizontal resolution of 18 km, is mesoscale resolving at low and midlatitudes. It has 50 vertical levels and employs the hydrostatic assumption. The model output used in this study covers the years 1992–2007 and is averaged every 3 days. The model realistically captures the overall spatial patterns of observed hydrographic and sea level variability, and the model data misfit is especially small in the upper ocean at mid/low latitudes.

b. Choice of regions and partition of energy reservoirs

Figure 2 shows the 16-yr average of total kinetic energy integrated over the entire water column. The kinetic energy is mainly concentrated in the equatorial regions, Southern Ocean, subtropical gyre regions, and western boundary currents and their extension regions. It is challenging to examine time-dependent energetics in the entire global ocean. Thus, we chose to focus on four energetic oceanic regions: the Kuroshio Extension (29°–42°N, 130°–170°E), the Gulf Stream Extension (29°–42°N, 78°–53°W), the Southern Ocean (65°–40°S), and a representative subtropical gyre patch in the North Pacific (10°–22°N, 150°E–135°W), indicated by the black boxes in Fig. 2. Results from the ECCO2 model presented next are not sensitive to a shift of the domain by 1°, which is on the eddy scale.

The time-dependent energy diagram contains six energy components: mean energy (P_M and K_M), eddy energy (P_E and K_E), and the energy anomaly residual (P_R and K_R). Figure 3 shows the histogram of K_E/K_M, K_R/K_M, P_E/P_M, and P_R/P_M in the four selected regions. The histogram characteristics vary greatly from region to region. For example, the K_E/K_M histogram is narrow in the Southern Ocean but wide in the Gulf Stream Extension region. Yet, these four regions also have similarities. First, most values of K_R/K_M and P_R/P_M lie within $[-1, 1]$, indicating the K_R magnitude is smaller than K_M and the P_R magnitude is smaller than P_M. Second, K_E is larger than K_M, but P_E is smaller than P_M, which is consistent with the results in von Storch et al. (2012).

c. Wind power input versus eddy–mean flow interactions

Several previous studies estimated the wind power input into the oceanic general circulation (e.g., Wunsch 1998; Scott and Xu 2009; Zhai et al. 2012). The total wind power input can be decomposed into three components:

$$W = \underbrace{\overline{\tau}_i \overline{u}_i}_{W_M} + \underbrace{\tau_i' u_i'}_{W_E} + \underbrace{\tau_i' \overline{u}_i + \overline{\tau}_i u_i'}_{W_R}, \tag{18}$$

where τ_i is the wind stress, and u_i is the horizontal velocity. Integrating the X terms in the K_M, K_E, and K_R equations [Eqs. (11)–(13)] throughout the water column and using the surface boundary conditions reveal that W_M, W_E, and W_R are the wind power input into K_M, K_E, and K_R, respectively. The surface boundary condition employed is

$$A_z \frac{\partial}{\partial z} \overline{u}_i = \overline{\tau}_i, \quad \text{and} \quad A_z \frac{\partial}{\partial z} u_i' = \tau_i', \tag{19}$$

where A_z is vertical viscosity. The term W_E/W_M is mostly positive; W_E/W_M is smaller than the one in the subtropical gyre and Southern Ocean but can be larger than

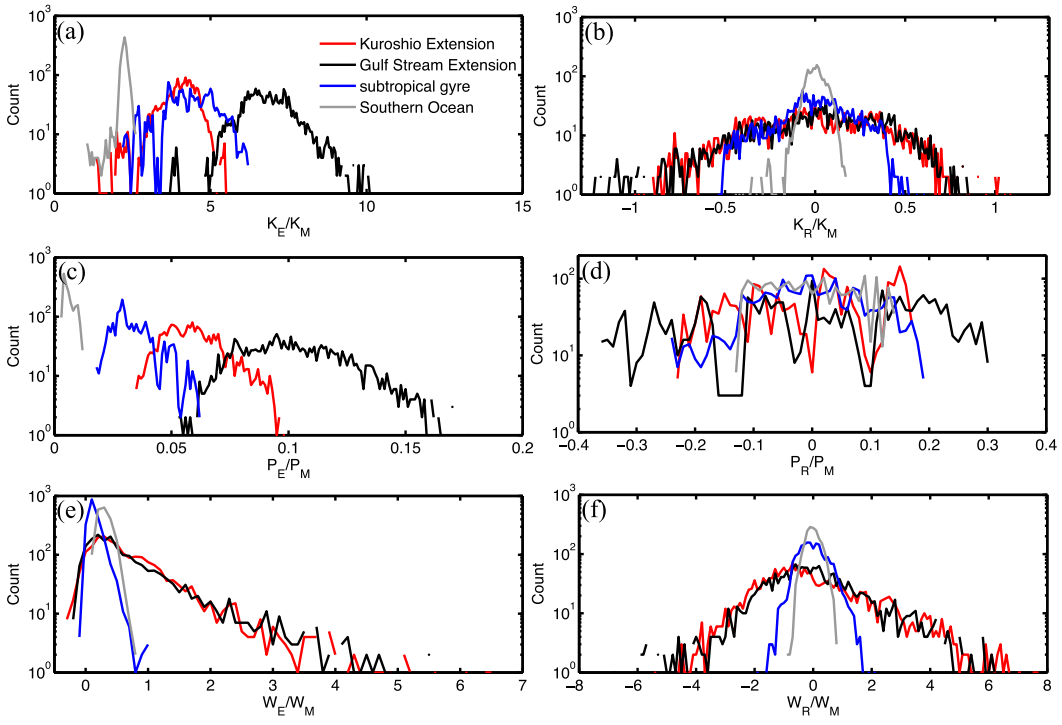

FIG. 3. Histogram of (a) K_E/K_M, (b) K_R/K_M, (c) P_E/P_M, (d) P_R/P_M, (e) W_E/W_M, and (f) W_R/W_M in the Kuroshio Extension, Gulf Stream Extension, subtropical gyre, and Southern Ocean regions, as indicated by the black boxes in Fig. 2. The terms K_E, K_R, and K_M are the three components of kinetic energy [Eqs. (1)–(4)]. The terms P_E, P_R, and P_M are the three components of available potential energy [Eqs. (7)–(10)]. The terms W_E, W_R, and W_M are the three components of wind power input [Eq. (18]. The histograms in (a)–(f) are sorted in 0.05, 0.01, 0.001, 0.01, 0.1, and 0.1 bins, respectively. The kinetic and potential energy time series used for the histogram analysis here are those integrated over the entire water column and the entire region.

the one in other regions (Fig. 3e). The W_R/W_M histogram centers at zero and spans from −5 to 5 (Fig. 3f).

Oceanic variability can be influenced by external forcing and at the same time modulated by nonlinear energy transfers (section 1). To assess how well the energy exchanges composing eddy–mean flow interactions (E terms) covary with the wind power input, we carried out coherence analysis between time series of the wind power input and E terms. Coherence analysis between two variables A and B, used in sections 3 and 4, can reveal how the two time series are similar in the frequency domain (e.g., Emery and Thomson 2004; Wunsch 2015). The amplitude reflects how much variability in variable A can be ascribed to variable B through a linear relation.

Take the Southern Ocean as an example: W_R is coherent with $E_{P_R \to K_R}$ at frequencies higher than 0.07 cycle day^{-1}, that is, periods shorter than 14 days, at the 95% confidence level (Fig. 4a). The coherence amplitude between W_R and all other E terms are statistically insignificant at the 95% confidence level at most available frequencies. The coherence between W_R and $E_{K_R \to K_E}$ is shown in Fig. 4b; other coherence plots are similar (not shown).

Table 2 shows the coherence between W_R and E terms in all the four selected regions. The number in this table denotes the percentage of available frequencies with significant coherence between W_R and the E term; the larger the percentage, the stronger is the coherence. In all the regions, W_R is highly coherent with $E_{P_R \to K_R}$ (percentage larger than 44%), indicating that the W_R variability is mostly tunneled to P_R through $E_{P_R \to K_R}$. However, the coherence between W_R and other E terms is low in the Southern Ocean and Kuroshio and Gulf Stream Extension regions (percentage lower than 17%), which may be because these regions are highly nonlinear and thus much variability is intrinsic arising from nonlinearity. The subtropical patch is less nonlinear than the other three regions (Chelton et al. 2011). Consistently, stronger coherence occurs there: the percentage is larger than 53% for all the E terms except $E_{P_R \to P_E}$ and $E_{P_E \to K_E}$, both of which are key during baroclinic instability.

As a comparison, we also carried out the coherence analysis between W_E and E terms in the four regions (not shown). The percentage of available frequencies at which the coherence amplitude is statistically significant

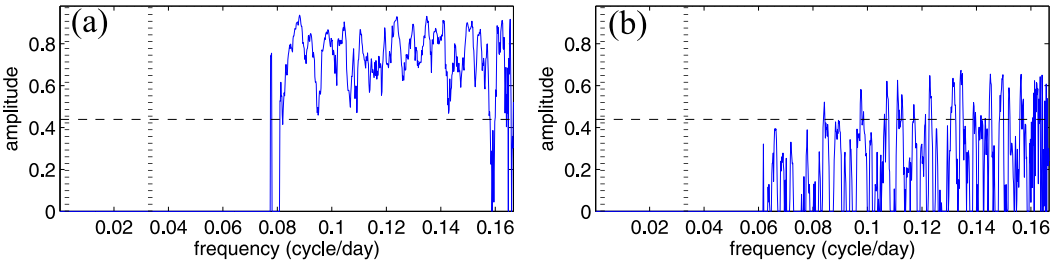

FIG. 4. The amplitude from the coherence analysis (a) between W_R and $E_{P_R \to K_R}$ and that (b) between the W_R and $E_{K_R \to K_E}$ in the Southern Ocean. The time series W_R, $E_{P_R \to K_R}$, and $E_{K_R \to K_E}$ used in the coherence analysis are those integrated over the entire Southern Ocean. Vertical dashed black lines indicate the frequencies of one cycle per year and one cycle per month. Horizontal dashed line indicates the 95% confidence level.

at the 95% confidence level is lower than 17% in almost all the cases. The only exception is the coherence between $E_{P_R \to P_E}$ and W_E in the Kuroshio Extension region. The percentage in this case reaches 28%.

4. Temporal coherence of eddy–mean flow interactions

This section examines how the energy exchange terms composing eddy–mean flow interactions are temporally coherent with each other. A delay phenomenon occurring during baroclinic instability and a suppression phenomenon occurring during mixed instability were identified (section 4a). The mechanism of the delay phenomenon is discussed in section 4b.

a. ECCO2 model results

1) DELAY PHENOMENON DURING BAROCLINIC INSTABILITY

From a time-mean perspective, in both the Southern Ocean and subtropical gyre regions, P_E and K_E gain energy primarily through baroclinic instability, and barotropic instability is negligible (Chen et al. 2014a). The coherence analysis between $E_{P_R \to P_E}$ and $E_{P_E \to K_E}$, which are key energy transfer terms during baroclinic instability, reveals a delay phenomenon. That is, during baroclinic instability, the P_E reservoir holds the energy transferred from P_R for some time period before transferring it to K_E.

As an example, Fig. 5a shows the coherence between $E_{P_R \to P_E}$ and $E_{P_E \to K_E}$ at 1000–2000 m in the Southern Ocean. At frequencies lower than 0.007 cycle day^{-1}, the coherence amplitude is statistically significant at the 95% confidence level, and the phase is slightly negative, with a mean value of −14°, indicating that the $E_{P_R \to P_E}$ variability leads the $E_{P_E \to K_E}$ variability at those frequencies. Dividing the phase in degrees by the corresponding frequency leads to the phase in days. At frequencies lower than one cycle per year, the phase ranges from −15° to −3°, corresponding to −94 to −3 days [Fig. 5a(2)]. That is, the delay time scale ranges from months to days for frequencies lower than one cycle per year in this case.

This delay phenomenon occurs, respectively, at upper 600 and 3000 m in the subtropical gyre and Southern Ocean regions, which are away from the ocean bottom (Figs. 6c,d). Figure 6 shows the phase (color) and amplitude, averaged over three frequency ranges, from the coherence analysis between $E_{P_R \to P_E}$ and $E_{P_E \to K_E}$ at each depth level. In the upper 600 m of the subtropical gyre and upper 3000 m in the Southern Ocean, the amplitudes for midfrequencies (1 cycle per year–1 cycle per month) and low frequencies (lower than 1 cycle per year) are statistically significant at the 95% confidence level at quite a few depth levels, and the phases are slightly negative at most depth levels with statistically significant amplitudes. Therefore, the $E_{P_R \to P_E}$ variability leads the $E_{P_E \to K_E}$ variability there.

Figures 6a and 6b are the same as Figs. 6c and 6d but for the Kuroshio and Gulf Stream Extensions. In these

TABLE 2. Coherence analysis was carried out between the W_R time series and each E term time series in the Kuroshio Extension (KE), Gulf Stream Extension (GSE), subtropical gyre (SG), and Southern Ocean (SO) regions. The first column shows the E term with which the coherence analysis of W_R was carried out. The other columns show the percentage of available frequencies at which the coherence amplitude is statistically significant at the 95% confidence level. The W_R and E term time series used in the coherence analysis are those integrated over each selected region.

E term	KE	GSE	SG	SO
$E_{P_R \to K_R}$	45%	72%	54%	50%
$E_{P_E \to K_E}$	11%	12%	9%	7%
$E_{K_R \to K_M}$	14%	10%	72%	13%
$E_{K_R \to K_E}$	9%	10%	55%	10%
$E_{P_R \to P_M}$	11%	16%	58%	9%
$E_{P_R \to P_E}$	11%	10%	9%	10%

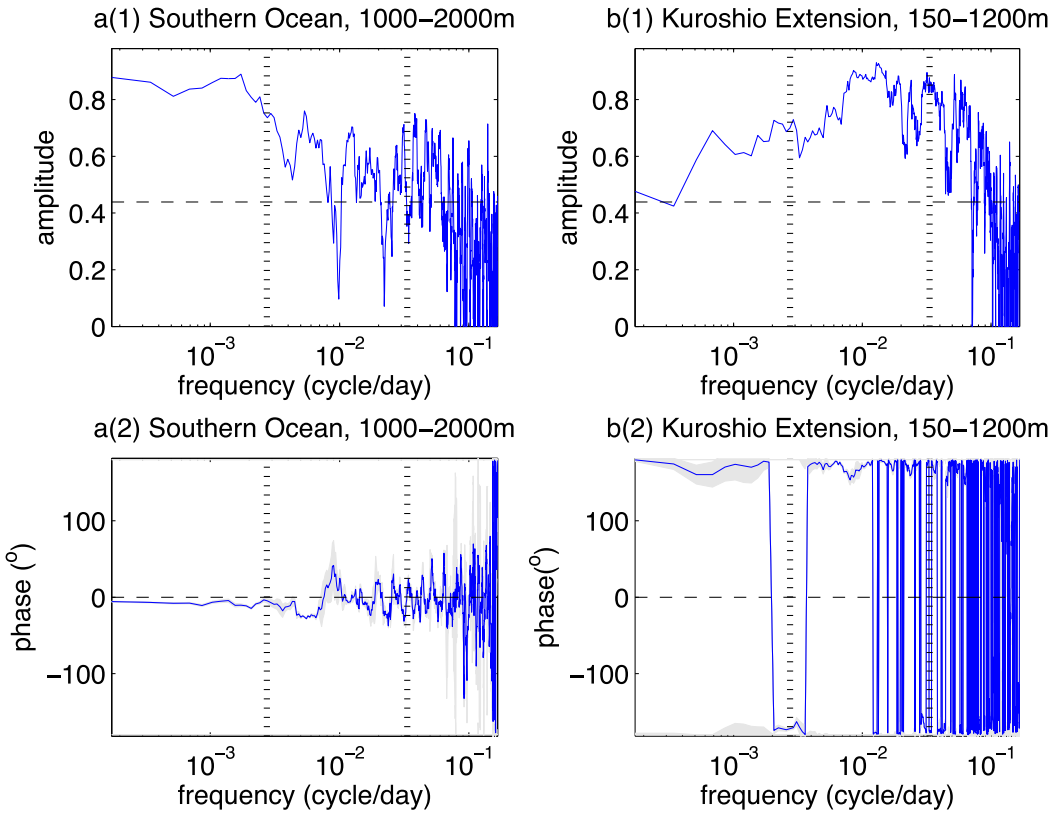

FIG. 5. (a) Coherence analysis between $E_{P_R \to P_E}$ integrated over 1000–2000 m and $E_{P_E \to K_E}$ at the same depth range in the Southern Ocean. (b) As in (a), but between $E_{K_R \to K_E}$ and $E_{P_E \to K_E}$ integrated over 150–1200 m in the Kuroshio Extension region. Top panels show amplitude and lower panels show phase. The negative phase at low frequencies in (a2) indicates that the $E_{P_R \to P_E}$ variability leads the $E_{P_E \to K_E}$ variability at those frequencies. In (b2), the phase amplitude at low frequencies is close to 180°, indicating that the increase (decrease) of $E_{K_R \to K_E}$ corresponds to the decrease (increase) of $E_{P_E \to K_E}$. Horizontal dashed black lines in (a1) and (b1) indicate the amplitude of no significance at 95% confidence level. Vertical dashed black lines correspond to the frequency one cycle per year and one cycle per month. Gray area in (a2) and (b2) indicates the error bar for phase at 95% confidence level.

two regions, statistically significant coherence between $E_{P_R \to P_E}$ and $E_{P_E \to K_E}$ also exists. However, most corresponding phases are slightly positive, indicating that the $E_{P_R \to P_E}$ variability lags the $E_{P_E \to K_E}$ variability, which is opposite those in the Southern Ocean and subtropical gyre. This may be related to the occurrence of the opposite process of baroclinic instability; in the downstream of the two extension regions, the mean jet is weak and eddies feed energy back to the mean flow (e.g., Waterman and Jayne 2011; Chen et al. 2014a). Instability occurs farther upstream in the two regions though, where the mean jet is intense and unstable (e.g., Waterman and Jayne 2011). The opposite process of instability also occurs downstream of meanders in the Southern Ocean (e.g., Johnson et al. 1992; Williams et al. 2007; Bischoff and Thompson 2014; Chapman et al. 2015), but its effect would be obscured by the fact that we performed a circumpolar average in the Southern Ocean.

2) SUPPRESSION PHENOMENON DURING MIXED INSTABILITY

Here, we discuss the relation between barotropic and baroclinic energy pathways to EKE during mixed instabilities. From a time-mean and domain average perspective, mixed barotropic and baroclinic instabilities occur in the Kuroshio and Gulf Stream Extensions; in contrast, barotropic instability is negligible as compared to baroclinic instability in the Southern Ocean and subtropical gyre regions (e.g., Kontoyiannis 1997; Chen et al. 2014a; Kang and Curchitser 2015). Thus, we focus on the Kuroshio and Gulf Stream Extensions.

Coherence analysis between the $E_{K_R \to K_E}$ and $E_{P_E \to K_E}$ time series reveals that a suppression phenomenon

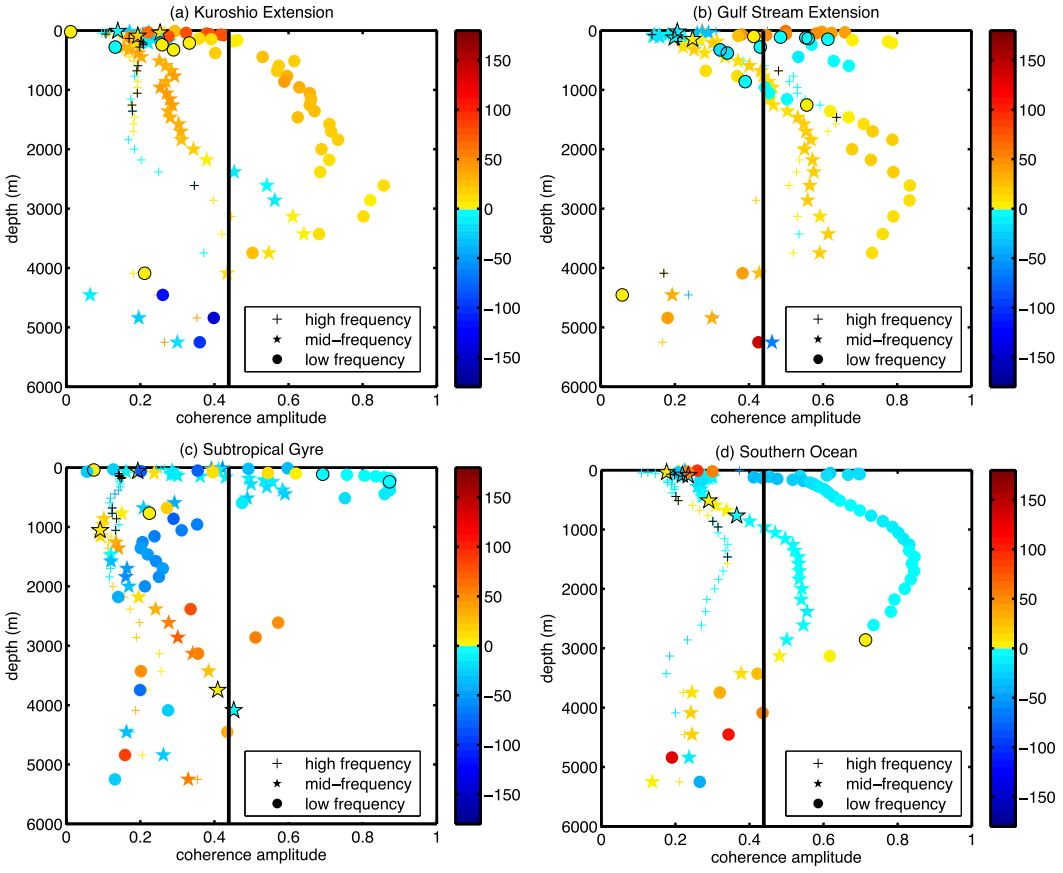

FIG. 6. Coherence analysis between $E_{P_R \to P_E}$ and $E_{P_E \to K_E}$ at each depth level in (a) the Kuroshio Extension, (b) Gulf Stream Extension, (c) subtropical gyre, and (d) Southern Ocean regions. The phase (color) and amplitudes from the coherence analysis shown here are the average over the high-frequency range (plus), midfrequency range (star), and low-frequency range (dot). The separation point between high and midfrequency is one cycle per month, and the separation point between mid- and low frequency is one cycle per year. Negative (positive) phase at a frequency indicates that the $E_{P_R \to P_E}$ variability leads (lags) the $E_{P_E \to K_E}$ variability at that frequency. Vertical black line indicates the amplitude of no significance at 95% confidence level. The markers with (without) black edges mean that the phase is indistinguishable (distinguishable) from zero at the 95% confidence level.

occurs in these two regions; when $E_{K_R \to K_E}$ decreases (increases), $E_{P_E \to K_E}$ increases (decreases; Figs. 5b, 7). That is, when the barotropic energy pathway weakens (strengthens), the baroclinic one strengthens (weakens). For example, at 150–1200 m in the Kuroshio Extension, $E_{K_R \to K_E}$ and $E_{P_E \to K_E}$ are significantly coherent with each other at the 95% confidence level at most frequencies, and the phase amplitude is close to 180°, indicating that $E_{K_R \to K_E}$ and $E_{P_E \to K_E}$ have a suppression relation (Fig. 5b). Figure 7 shows the absolute value of the phase (color) and the coherence amplitude, averaged over three frequency ranges, from the coherence analysis between $E_{K_R \to K_E}$ and $E_{P_E \to K_E}$. In both regions, the amplitudes at middepth are statistically significant at the 95% confidence level for both mid- and low frequencies. All those coherence amplitudes that are statistically significant have phase magnitudes close to 180°, which corresponds to a suppression relation between $E_{K_R \to K_E}$ and $E_{P_E \to K_E}$. Further discussion about this phenomenon is in section 5.

b. *Quasigeostrophic model results: Delay phenomenon and its mechanism*

There are many interesting results from the ECCO2 model that could be pursued; however, in the following section, we adopt a simpler model to provide further mechanistic insight into the delay phenomenon discussed in section 4a(1).

1) MODEL SETUP AND EQUILIBRATED STATE

A two-layer, QG model on a beta plane (e.g., Phillips 1954; Pedlosky 1987; Panetta 1993) is employed. This model, in appropriate parameter regimes, proves to be reasonable for eddy/jet studies in both the midlatitude ocean interior and Southern Ocean (e.g., Arbic 2000;

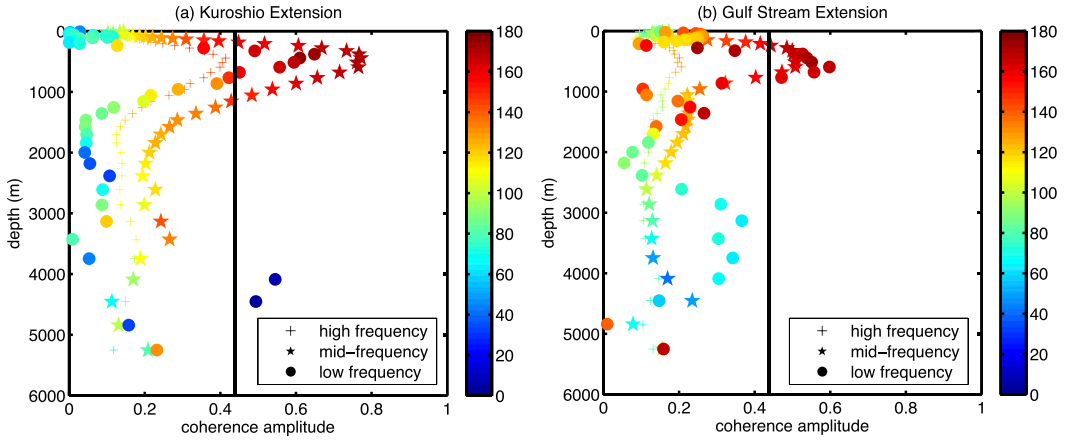

FIG. 7. Coherence analysis between $E_{K_R \to K_E}$ and $E_{P_E \to K_E}$ at each depth level in (a) the Kuroshio Extension and (b) Gulf Stream Extension regions. The absolute value of the phase (color) and amplitude from the coherence analysis are the average over the high-frequency range (plus), midfrequency range (star), and low-frequency range (dot). The separation point between high- and midfrequency is one cycle per month, and the separation point between mid- and low frequency is one cycle per year. The vertical black line indicates the amplitude of no significance at the 95% confidence level. The phase amplitudes in (a) and (b) are all distinguishable from zero at the 95% confidence level.

Thompson 2010; Venaille et al. 2011). The eddy potential vorticity (PV) satisfies

$$\left(\frac{\partial}{\partial t} + U_i \frac{\partial}{\partial x}\right) q_i + J(\phi_i, q_i + \overline{q_i}) = -r\delta_{i2}\nabla^2\phi_2, \quad (20)$$

where ϕ_i, q_i, $\overline{q}_i$, and U_i are eddy streamfunction, eddy PV, mean PV, and the imposed zonal mean flow in the upper ($i = 1$) and lower ($i = 2$) layers. Here, δ_{ij} is the Kronecker delta, and r is the bottom friction coefficient. The eddy PV and mean PV are respectively defined as

$$q_i = \nabla^2\phi_i + (-1)^i F_i(\phi_1 - \phi_2) \quad \text{and}$$
$$\overline{q}_i = \beta y - (-1)^i F_i(U_1 y - U_2 y). \quad (21)$$

The term $F_i = f_0^2/(\gamma_1 H_i) = [1 + \delta_{i2}(\delta - 1)]/[(1 + \delta)R_d^2]$, where $\gamma_1 = g(\rho_2 - \rho_1)/\rho_0$ is the reduced gravity, $R_d = 1/\sqrt{F_1 + F_2}$ is the deformation radius, and $\delta = H_1/H_2$ is the ratio between the upper- and lower-layer thickness. The Coriolis parameter and the meridional gradient of planetary vorticity are represented by f_0 and β. The model is solved numerically in a double periodic domain using the pseudospectral method, and small-scale variability is damped using a wavenumber cutoff filter (Arbic 2000).

Parameters' values in the control run are representative of the midlatitude ocean. The domain is discretized into 256×256 grids, with the size of 1000 km $\times$ 1000 km. The deformation radius R_d is 40 km, r is 0.08 day^{-1}, and values of f_0 and β at 40°N were employed. Assuming the upper- and lower-layer interface is the thermocline, δ is the ratio between the thermocline depth and the total ocean depth, and it is chosen to be 0.2. The imposed mean flow is $U_1 = -U_2 = 10\,\text{km day}^{-1} \approx 0.1\,\text{m s}^{-1}$. In this case, the maximum growth rate $\sigma_{\max}$, calculated using the linear stability analysis approach in Arbic (2000), is 1/46 day^{-1}, consistent with the baroclinic growth rate in the west Pacific and east Pacific regions (Tulloch et al. 2011). The initial condition is small-amplitude random motions with the dominant size of 140 km.

Our analysis is mainly based on the 10-yr output at 0.25-day interval from the equilibrated state of the control run (Figs. 8–13), though experiments with different choices of δ and mean vertical shear were carried out for exploring the delay time scale (Fig. 14). The time series of energy content in various reservoirs in the control run and their spectra are shown in Fig. 8. The QG model is consistent with the ECCO2 model in that the energy spectra are red and cover all available frequencies, though the seasonal cycle does not exist in the QG spectra. Compared to the ECCO2 model, the QG model not only has no seasonal cycle but also lacks wind, topography, coastline, and continuous stratification. Yet, the delay phenomenon occurs in the QG model [section 4b(2)], indicating that this simple model includes the essential physics producing the delay.

2) ENERGY PATHWAYS AND DELAY PHENOMENON

The equation for the total eddy energy in the QG two-layer model has been previously discussed (e.g., Arbic

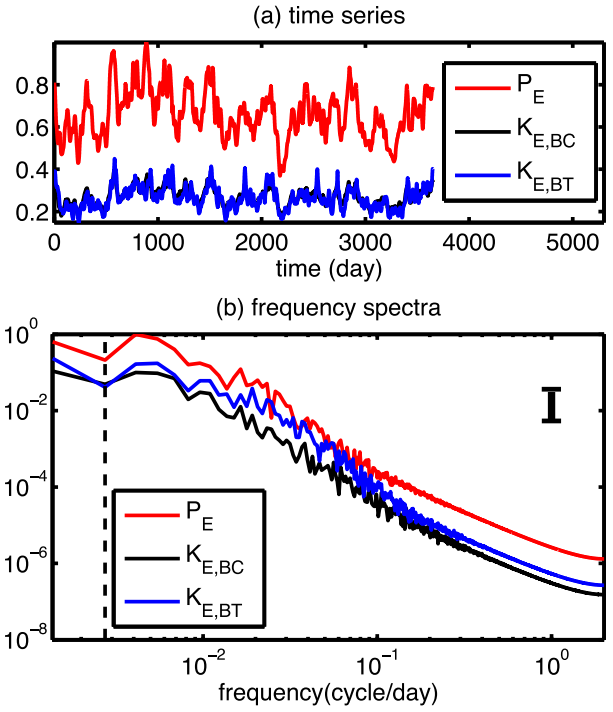

FIG. 8. (a) The 10-yr time series of $\langle P_E\rangle$, $\langle K_{E,\mathrm{BC}}\rangle$, and $\langle K_{E,\mathrm{BT}}\rangle$ in the equilibrated state from the control experiment using the QG model. The time series shown here is normalized by the maximum value of these three time series. The black line, which represents $\langle K_{E,\mathrm{BC}}\rangle$, is under the blue line, corresponding to $\langle K_{E,\mathrm{BT}}\rangle$. (b) The frequency spectra of the $\langle P_E\rangle$, $\langle K_{E,\mathrm{BC}}\rangle$, and $\langle K_{E,\mathrm{BT}}\rangle$ time series, normalized by the maximum value of the three spectra. The error bar denotes spectral uncertainties at 95% confidence level, and the dashed line indicates the frequency one cycle per year.

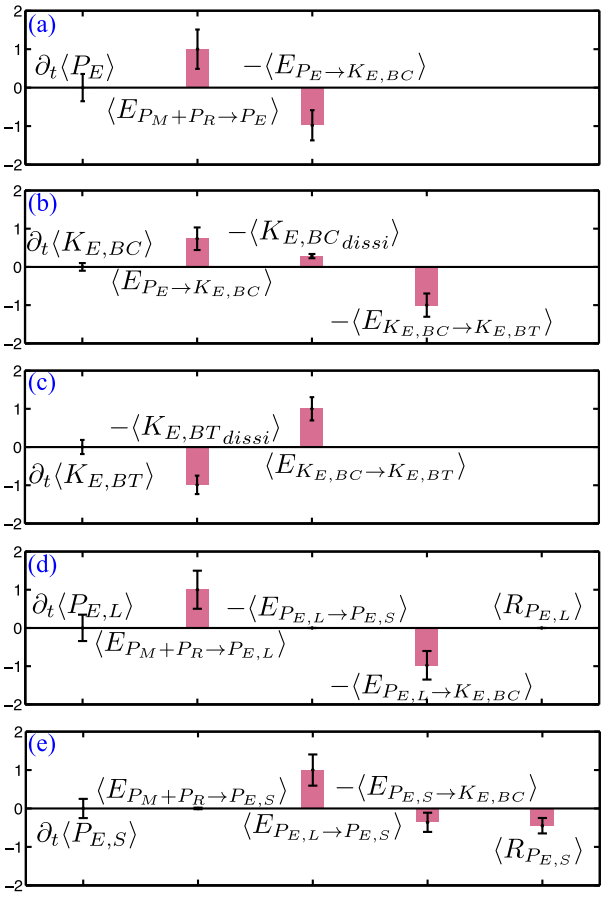

FIG. 9. The normalized energy budgets of (a) $\langle P_E\rangle$, (b) $\langle K_{E,\mathrm{BC}}\rangle$, (c) $\langle K_{E,\mathrm{BT}}\rangle$, (d) $\langle P_{E,L}\rangle$, and (e) $\langle P_{E,S}\rangle$ in the control run, using Eqs. (23)–(25), (30), and (31). The vertical bars in purple denote the time mean of each term. The black error bars are one standard deviation of each term, which can indicate the amplitude of the temporal variability. The time mean and standard deviation of each term shown here is normalized by the maximum absolute value of all the terms in each budget.

2000; Thompson and Young 2006). Here, we provide equations for $P_M + P_R$ and the three components of eddy energy, that is, the potential energy P_E, baroclinic EKE $K_{E,\mathrm{BC}}$, and barotropic EKE $K_{E,\mathrm{BT}}$:

$$\frac{\partial}{\partial t}\langle P_M + P_R\rangle = \frac{\partial}{\partial t}\langle P_R\rangle = \langle E_{K_M+K_R\to P_M+P_R}\rangle - \langle E_{P_M+P_R\to P_E}\rangle, \quad (22)$$

$$\frac{\partial}{\partial t}\langle P_E\rangle = \langle E_{P_M+P_R\to P_E}\rangle - \langle E_{P_E\to K_{E,\mathrm{BC}}}\rangle, \quad (23)$$

$$\frac{\partial}{\partial t}\langle K_{E,\mathrm{BC}}\rangle = \langle E_{P_E\to K_{E,\mathrm{BC}}}\rangle - \langle K_{E,\mathrm{BC}_{\mathrm{dissi}}}\rangle - \langle E_{K_{E,\mathrm{BC}}\to K_{E,\mathrm{BT}}}\rangle, \quad \text{and} \quad (24)$$

$$\frac{\partial}{\partial t}\langle K_{E,\mathrm{BT}}\rangle = -\langle K_{E,\mathrm{BT}_{\mathrm{dissi}}}\rangle + \langle E_{K_{E,\mathrm{BC}}\to K_{E,\mathrm{BT}}}\rangle. \quad (25)$$

Here, $\langle\cdot\rangle$ means the spatial average over the double periodic domain, $E_{a\to b}$ is the eddy energy conversion rate from the reservoir a to the reservoir b, and $K_{E,\mathrm{BC}_{\mathrm{dissi}}}$ and $K_{E,\mathrm{BT}_{\mathrm{dissi}}}$ denote the energy change rate due to bottom friction. The mathematical forms of P_E, $K_{E,\mathrm{BC}}$, and $K_{E,\mathrm{BT}}$ and the derivation of Eqs. (22)–(25) are in appendix B.

Figure 10a is the time-dependent energy diagram diagnosed from Eqs. (22)–(25). In the control run, $\langle E_{P_M+P_R\to P_E}\rangle$, $\langle E_{P_E\to K_{E,\mathrm{BC}}}\rangle$, and $\langle E_{K_{E,\mathrm{BC}}\to K_{E,\mathrm{BT}}}\rangle$ are all positive (Fig. 9). In fact, they are also positive at every snapshot (not shown). Therefore, baroclinic instability and barotropization occur, and the energy pathway is

$$\langle P_M + P_R\rangle \to \langle P_E\rangle \to \langle K_{E,\mathrm{BC}}\rangle \to \langle K_{E,\mathrm{BT}}\rangle. \quad (26)$$

It is known that, in the baroclinically unstable system, P_E is converted to K_E (Pedlosky 1987). Here, the energy transfer from P_E to K_E is through the vertical motion of the upper–lower-layer interface, which is absent in the

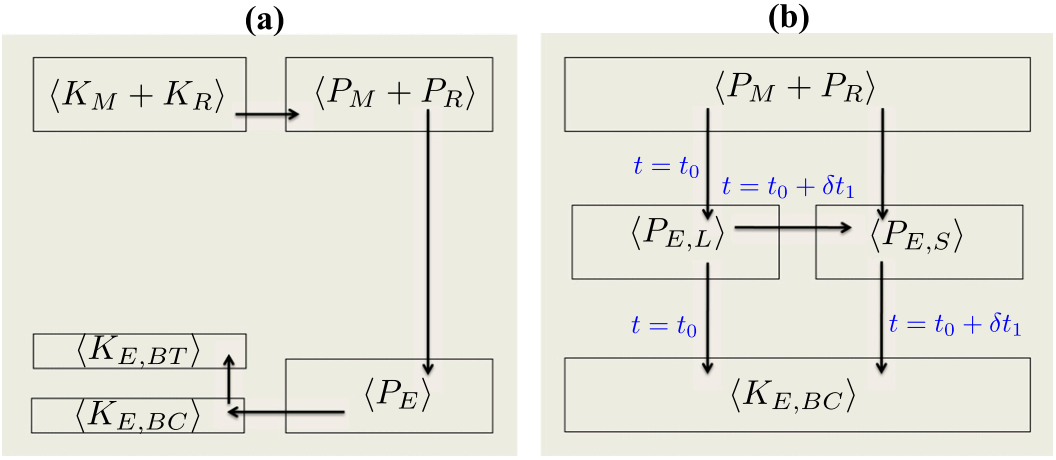

FIG. 10. The energy diagrams summarizing the energy budget diagnosed from (a) the double decomposition framework [Eqs. (22)–(25)] and (b) the triple decomposition framework [Eqs. (30)–(31)]. Double decomposition means that the total flow is divided into two components: mean flow and eddies. Triple decomposition means that the total flow is divided into three components: mean, large-scale eddies, and small-scale eddies. The arrow direction is determined from diagnosing the energy budgets. The time information in (b) is based on the correlation results shown in Fig. 13. In (b), after the potential energy is transferred from the mean flow to large-scale eddies at $t = t_0$ (i.e., transferred from $P_M + P_R$ to $P_{E,L}$), some of it is further converted to kinetic energy immediately (i.e., transfer from $P_{E,L}$ to $K_{E,\mathrm{BC}}$). However, some other part of the potential energy cascades to small-scale eddies first (i.e., transfer from $P_{E,L}$ to $P_{E,S}$), before converting to kinetic energy. The delay δt_1 occurs when energy cascades from $P_{E,L}$ to $P_{E,S}$.

barotropic relative vorticity equation. Thus, P_E is directly converted to the baroclinic mode $K_{E,\mathrm{BC}}$, not to the barotropic mode $K_{E,\mathrm{BT}}$. Energy in the $K_{E,\mathrm{BC}}$ reservoir is then transferred to $K_{E,\mathrm{BT}}$, which is due to the coupling between barotropic and baroclinic modes. For example, the advection of baroclinic (barotropic) vorticity by barotropic (baroclinic) motions can influence baroclinic motions [Eq. (B3)]. Although $K_{E,\mathrm{BT}}$ loses energy through bottom friction, bottom friction tends to decrease eddy velocity in the lower layer and thus increase the vertical shear and $\langle K_{E,\mathrm{BC}} \rangle$ (Fig. 9).

Compared to the energy diagram for the ECCO2 model (Fig. 1a), Fig. 10a is less complex: $\langle K_R \rangle$ in the QG model is zero due to the double periodic boundary condition; the energy exchange between $\langle K_M + K_R \rangle$ and $\langle K_E \rangle$ is zero because the imposed mean flow has no horizontal shear and no barotropic instability occurs. We chose not to separate P_M and P_R in Fig. 10a because the mean flow in the QG model is explicitly imposed and thus there is no explicit governing equation for the mean flow, making deriving the P_R and P_M equations a challenge.

The delay phenomenon, identified from the ECCO2 model, also exists in the QG model. We carried out coherence analysis between the energy exchange terms $E_{P_M+P_R \to P_E}$ and $E_{P_E \to K_{E,\mathrm{BC}}}$ (Figs. 11a,b). Similar to the

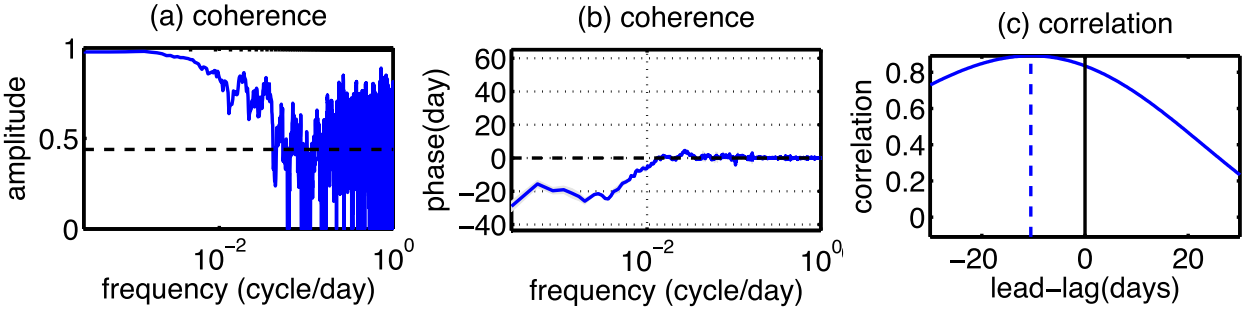

FIG. 11. The (a) amplitude and (b) phase in days from the coherence analysis between $\langle E_{P_M+P_R \to P_E} \rangle$ and $\langle E_{P_E \to K_{E,\mathrm{BC}}} \rangle$. The lead–lag correlation (c) between the low-pass filtered $\langle E_{P_M+P_R \to P_E} \rangle$ and $\langle E_{P_E \to K_{E,\mathrm{BC}}} \rangle$ (blue). The filter here removes temporal variability with frequencies higher than 10^{-2} cycle per day. The horizontal dashed black line in (a) and the gray area in (b) indicate the 95% confidence limits. Dashed vertical line in (c) indicates the lead–lag time at the maximum correlation value. The solid black vertical line in (c) indicates the zero lead–lag.

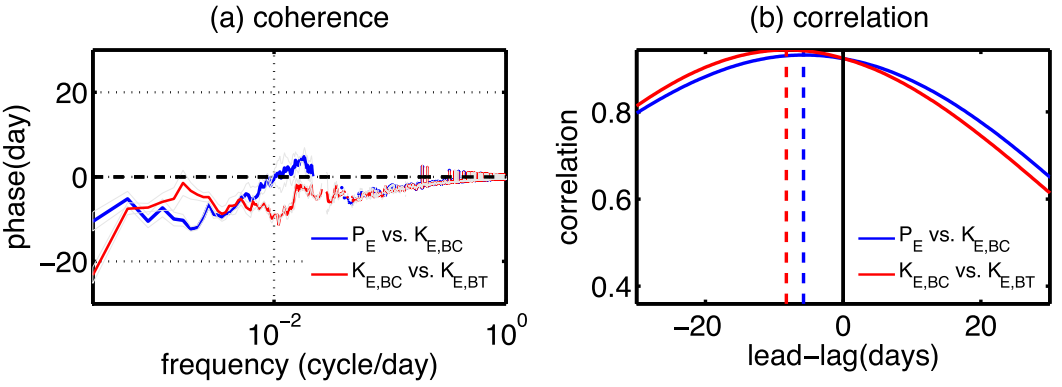

FIG. 12. (a) The phase in days from the coherence analysis and (b) the lead–lag correlation between $\langle P_E \rangle$ and $\langle K_{E,BC} \rangle$ (blue) and that between $\langle K_{E,BC} \rangle$ and $\langle K_{E,BT} \rangle$ (red). The gray lines in (a) indicates the 95% confidence limits. In (a), only phase at frequencies with statistically significant coherence amplitude is shown. Dashed vertical lines in (b) indicate the lead–lag time at the maximum correlation value. The solid black vertical line in (b) indicates the zero lead–lag. Correlations in (b) were diagnosed using the low-pass filtered time series, which only keeps variability at frequencies lower than 10^{-2} cycle per day.

ECCO2 model results (Figs. 5a, 6c,d), the coherence amplitude here is statistically significant at low frequencies, which denotes those lower than 0.01 cycle day^{-1} in this case. The corresponding phase is negative, indicating that $E_{P_M+P_R\to P_E}$ leads $E_{P_E\to K_{E,BC}}$ at these frequencies. Although correlation analysis does not reveal exactly the same information as coherence analysis, these two methods are connected from an application perspective. That is, both methods provide the lead–lag information. One can determine whether one time series leads another time series at a selected frequency from the phase of the coherence analysis. Similarly, one can evaluate whether a time series leads or lags another time series by identifying the lead–lag time at the maximum correlation value. Unsurprisingly, the correlation analysis also confirms that the delay phenomenon occurs: the lead–lag time is negative at the maximum correlation coefficient (Fig. 11c).

The coherence and correlation analyses between different energy reservoirs (Fig. 12) indicate that, besides the delay between the energy exchange terms $E_{P_M+P_R\to P_E}$ and $E_{P_E\to K_{E,BC}}$, a delay also occurs as the energy variability flows through the energy pathway chain [Eq. (26)]. Specifically, the P_E variability leads the $K_{E,BC}$ variability, and the $K_{E,BC}$ variability leads the $K_{E,BT}$ variability. At frequencies lower than 0.01 cycle per day, the coherence amplitude is statistically significant; the phase between P_E and $K_{E,BC}$ ranges from −13° to 0°, corresponding to −12 to 0 days, and the phase between $K_{E,BC}$ and $K_{E,BT}$ ranges from −34° to −1°, corresponding to −23 to −1 days (Fig. 12a). Consistently, the lead–lag time at the maximum correlation coefficient is negative, which also confirms the delay of energy flow in the energy pathway chain (Fig. 12b).

3) MECHANISM FOR THE DELAY PHENOMENON: LINEAR STABILITY ANALYSIS

Assuming ϕ_i has the normal-mode form,

$$\begin{aligned}\phi_i &= \mathrm{Re}[\tilde{\phi}_i e^{ik(x-c_1t-ic_2t)+ily}]\\ &= e^{kc_2t}\mathrm{Re}[\tilde{\phi}_i e^{ik(x-c_1t)+ily}].\end{aligned} \tag{27}$$

Define $\phi_i e^{-kc_2t} = a_i\cos\theta + b_i\sin\theta$, where c_2, a_i, and b_i are functions of k and l, and $\theta = kx - kc_1t + ly$. Then, we have

$$\begin{aligned}\langle P_E\rangle &= \frac{1}{2(1+\delta)}\langle F_2(\phi_1-\phi_2)^2\rangle\\ &= \frac{F_2}{4(1+\delta)}e^{2kc_2t}[(a_1-a_2)^2+(b_1-b_2)^2],\end{aligned} \tag{28}$$

$$\begin{aligned}\langle K_{E,BT}\rangle &= \frac{1}{2}\langle\nabla\phi_{BT}\cdot\nabla\phi_{BT}\rangle\\ &= \frac{(k^2+l^2)e^{2kc_2t}}{4(1+\delta)^2}[(a_1\delta+a_2)^2+(b_1\delta+b_2)^2],\\ \langle K_{E,BC}\rangle &= \frac{1}{2}\langle\nabla\phi_{BC}\cdot\nabla\phi_{BC}\rangle\\ &= \frac{(k^2+l^2)e^{2kc_2t}}{4(1+\delta)^2}[\delta(a_1-a_2)^2+\delta(b_1-b_2)^2],\end{aligned}$$

where ϕ_{BT} and ϕ_{BC} are defined in appendix B, section a. Therefore, if only a single wave is included in the linear system, all the energy reservoirs grow exponentially with the same growth rate. In this case, the delay does not occur, although the energy terms are coherent. If the initial condition is a single wave, the nonlinear terms are always zero in the QG two-layer model.

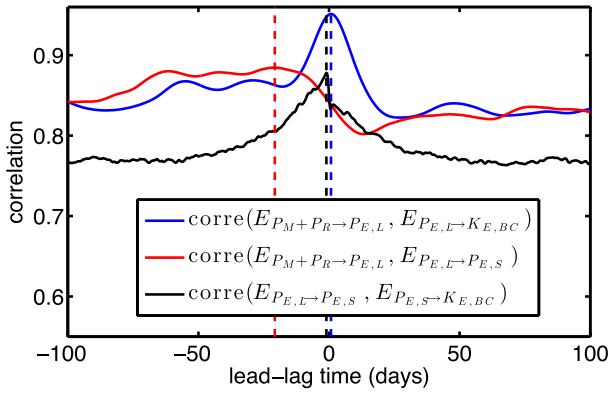

FIG. 13. Lead–lag correlations between $\langle E_{P_M+P_R\to P_{E,L}}\rangle$ and $\langle E_{P_{E,L}\to K_{E,BC}}\rangle$ (blue), between $\langle E_{P_M+P_R\to P_{E,L}}\rangle$ and $\langle E_{P_{E,L}\to P_{E,S}}\rangle$ (red), and between $\langle E_{P_{E,L}\to P_{E,S}}\rangle$ and $\langle E_{P_{E,S}\to K_{E,BC}}\rangle$ (black). Dashed vertical lines indicate the lead–lag time at the maximum correlation value.

4) MECHANISM FOR THE DELAY PHENOMENON: NONLINEAR ENERGY DIAGNOSIS

The absence of the delay phenomenon in the normal-mode linear analysis indicates eddy–eddy interaction may be key for the delay. "Triple decomposition," a simple method to evaluate eddy–eddy interaction, refers to decomposing an arbitrary variable a at the position $\mathbf{x}$ and time t into three parts:

$$a(\mathbf{x},t)=\overline{a}(\mathbf{x})+a'_L(\mathbf{x},t)+a'_S(\mathbf{x},t), \tag{29}$$

where $\cdot_L$ and $\cdot_S$ are, respectively, the large- and small-scale spatial filter, and $\overline{\cdot}$ denotes the time mean. The separation point between large and small scales is arbitrary. Though a spectral gap assumption is employed in previous studies using triple decomposition (e.g., Davis 1994; Ferrari and Polzin 2005), closing the energy budgets is important for the purpose here. Thus, we use the P_E equations without the spectral gap assumption:

$$\frac{\partial}{\partial t}\langle P_{E,L}\rangle=\langle E_{P_M+P_R\to P_{E,L}}\rangle-\langle E_{P_{E,L}\to K_{E,\mathrm{BC}}}\rangle-\langle E_{P_{E,L}\to P_{E,S}}\rangle+\langle R_{P_{E,L}}\rangle, \quad \text{and} \tag{30}$$

$$\frac{\partial}{\partial t}\langle P_{E,S}\rangle=\langle E_{P_M+P_R\to P_{E,S}}\rangle-\langle E_{P_{E,S}\to K_{E,\mathrm{BC}}}\rangle+\langle E_{P_{E,L}\to P_{E,S}}\rangle+\langle R_{P_{E,S}}\rangle, \tag{31}$$

where $P_{E,L}$ and $P_{E,S}$ are the APE in large- and small-scale eddies, respectively, and $K_{E,\mathrm{BC},L}$ and $K_{E,\mathrm{BC},S}$ are the K_E in large- and small-scale baroclinic eddies, respectively. As stated in sections 2b and 4b(2), $E_{a\to b}$ is the energy conversion rate from reservoir a to reservoir b; $R_{P_{E,L}}$ and $R_{P_{E,S}}$, respectively, denote the energy transfer between $P_{E,L}$ and the residue P_E and that between $P_{E,S}$ and the residue P_E. The residue P_E, arising from the lack of separation between motions at different spatial scales, denotes the difference between total P_E and $P_{E,L}+P_{E,S}$ [Eqs. (B12)]. Details are in appendix B, section c.

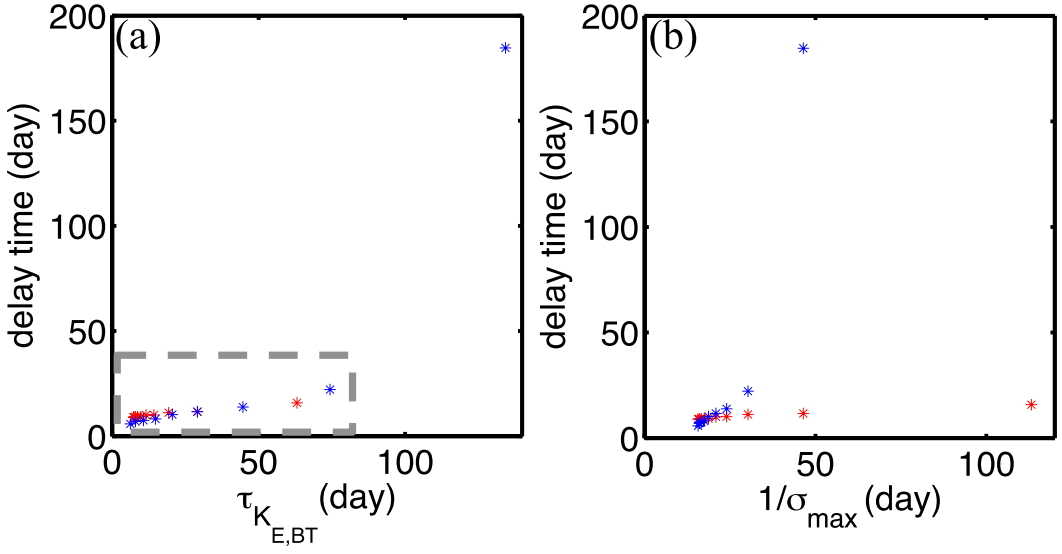

FIG. 14. (a) Scatterplot between the delay time and the barotropic eddy turnover time scale $\tau_{K_{E,\mathrm{BT}}}$. (b) Scatterplot between the delay time and $1/\sigma_{\max}$, where $\sigma_{\max}$ is the maximum growth rate diagnosed using the linear stability analysis approach from Arbic (2000). The delay time here refers to the days that $\langle P_E\rangle$ leads $\langle K_{E,\mathrm{BT}}\rangle$. Red stars are results from the group of experiments with varying δ; blue stars show results from the group of experiments with varying vertical shear. The dashed gray box in (a) shows the parameter space where the delay time and $\tau_{K_{E,\mathrm{BT}}}$ roughly satisfies a linear relation.

Figures 9d and 9e show the energy budgets of $\langle P_{E,L}\rangle$ and $\langle P_{E,S}\rangle$. The time mean and standard deviation of each term are illustrated by the vertical bar in purple and the error bar in black, respectively. The sum of the time mean and standard deviation indicates the magnitude of each term at every snapshot. The separation point between large and small scales in Figs. 9d and 9e is 354 km. However, results are not qualitatively sensitive to the choice of separation scale ranging from 40 to 490 km. The $\langle P_{E,L}\rangle$ budget is approximately

$$\frac{\partial}{\partial t}\langle P_{E,L}\rangle \approx \langle E_{P_M+P_R\to P_{E,L}}\rangle - \langle E_{P_{E,L}\to K_{E,\mathrm{BC}}}\rangle, \quad (32)$$

that is, the temporal variability of $\langle P_{E,L}\rangle$ is controlled by the energy conversion from $\langle P_M + P_R\rangle$ to $\langle P_{E,L}\rangle$ and the conversion from $\langle P_{E,L}\rangle$ to $\langle K_{E,\mathrm{BC},L}\rangle$. Since the large-scale density fronts store much more P_E than small-scale density fronts, the loss of $\langle P_{E,L}\rangle$ to $\langle P_{E,S}\rangle$ is negligible in the $\langle P_{E,L}\rangle$ budget. From a domain integral perspective, the energy transfer direction has no temporal variability (not shown). The $\langle P_{E,S}\rangle$ budget is approximately

$$\frac{\partial}{\partial t}\langle P_{E,S}\rangle \approx -\langle E_{P_{E,S}\to K_{E,\mathrm{BC}}}\rangle + \langle E_{P_{E,L}\to P_{E,S}}\rangle + \langle R_{P_{E,S}}\rangle. \quad (33)$$

The $\langle P_{E,S}\rangle$ budget has more high-frequency variability than the $\langle P_{E,L}\rangle$ budget. The stirring of the large-scale density fronts by eddy motions causes small-scale density fronts. Thus, energy is transferred from $P_{E,L}$ to $P_{E,S}$ through the term $E_{P_{E,L}\to P_{E,S}}$. The $P_{E,S}$ reservoir gets much more energy directly from vertical shear in large-scale eddy motions $P_{E,L}$ than from the imposed mean flow shear P_M. Part of the energy in the small-scale vertical shear $P_{E,S}$ is transferred to EKE through $E_{P_{E,S}\to K_{E,\mathrm{BC},S}}$.

The lead–lag correlation analysis reveals where the delay occurs (Fig. 13). The lead–lag time at the maximum correlation between $E_{P_M+P_R\to P_{E,L}}$ and $E_{P_{E,L}\to K_{E,\mathrm{BC}}}$ is roughly zero and so is the lead–lag time at the maximum correlation between $E_{P_{E,L}\to P_{E,S}}$ and $E_{P_{E,S}\to K_{E,\mathrm{BC}}}$. However, the $E_{P_M+P_R\to P_{E,L}}$ variability leads the $E_{P_{E,L}\to P_{E,S}}$ variability by roughly 20 days. That is, after $P_{E,L}$ obtains some extra energy from $P_M + P_R$, it immediately transfers part of it to $K_{E,\mathrm{BC}}$; however, it takes some time for the energy to be transferred from $P_{E,L}$ to $P_{E,S}$. After $P_{E,S}$ gets this extra energy, it is immediately transferred to $K_{E,\mathrm{BC}}$.

Figure 10b summarizes the triple decomposition results: $P_{E,L}$ gets energy from $P_M + P_R$ and then transfers part of it to $P_{E,S}$ and $K_{E,\mathrm{BC}}$; $P_{E,S}$ can get energy from both $P_{E,L}$ and $P_M + P_R$ and converts part of it to $K_{E,\mathrm{BC}}$. The transfer of energy from $P_{E,L}$ to $P_{E,S}$ is due to the forward cascade of P_E, which is consistent with the dual cascade scenario in Salmon (1980). The delay between the P_E and $K_{E,\mathrm{BC}}$ variability occurs because the P_E variability at large scales needs to be transferred to small-scale density fronts through energy cascades. As previously stated, the separation point between small and large scales is arbitrary, and the results described in Fig. 10b hold for separation scales ranging from the deformation radius to an order of magnitude higher. A delay also occurs between $K_{E,\mathrm{BC}}$ and $K_{E,\mathrm{BT}}$ (Fig. 12), whose origin may be related to the forward cascade of $K_{E,\mathrm{BC}}$.

5) Sensitivity analysis: Estimates of the delay time scale

The existence of the delay is related to the forward cascade of P_E [section 4b(4)]. The P_E cascade is through the stirring of density (buoyancy) fronts by eddies, that is, through $J(\phi_1, \phi_2)$ in the buoyancy equation [Eq. (B2)]. Since

$$J(\phi_1,\phi_2) = -\frac{1+\delta}{\sqrt{\delta}}J(\phi_{\mathrm{BT}},\phi_{\mathrm{BC}}), \quad (34)$$

density in this model is essentially advected by barotropic, not baroclinic, eddies. Note that the time scale for the energy cascade is roughly the eddy turnover time (Vallis 2006). Therefore, the delay time scale may be related to the barotropic eddy turnover time scale:

$$\tau_{K_{E,\mathrm{BT}}} = \frac{L_{K_{E,\mathrm{BT}}}}{\sqrt{\langle K_{E,\mathrm{BT}}\rangle}}, \quad (35)$$

where $L_{K_{E,\mathrm{BT}}}$ is the barotropic eddy length scale defined as the reciprocal of the $K_{E,\mathrm{BT}}$ spectrum centroid

$$L_{K_{E,\mathrm{BT}}} = \frac{2\pi\iint S_{K_{E,\mathrm{BT}}}(k,l)\,dk\,dl}{\iint S_{K_{E,\mathrm{BT}}}(k,l)\sqrt{k^2+l^2}\,dk\,dl}. \quad (36)$$

Here, k and l are the zonal and meridional wavenumbers, and $S_{K_{E,\mathrm{BT}}}$ is the $K_{E,\mathrm{BT}}$ spectrum.

To test whether the barotropic eddy turnover time scale $\tau_{K_{E,\mathrm{BT}}}$ is a good indicator of the delay time, we carried out sensitivity experiments: δ varies between 0.1 and 1 in one group and U_1 (i.e., $-U_2$) varies between 4 and 20 km day^{-1} in the other group. Other parameters, however, are the same as the control run. In these experiments, the delay time scale increases with $\tau_{K_{E,\mathrm{BT}}}$, and these two time scales have the same order of magnitude (Fig. 14a), indicating that $\tau_{K_{E,\mathrm{BT}}}$ is a proper indicator of the delay time scale overall. In the dashed gray box, where $\tau_{K_{E,\mathrm{BT}}}$ is smaller than 100 days, the relation between the delay time scale and $\tau_{K_{E,\mathrm{BT}}}$ is roughly linear. However, there is a star marker outside of the dashed gray box deviating from the linear fit, which corresponds to the experiment

with weak vertical shear ($U_1 = -U_2 = 4\,\mathrm{km\,day^{-1}}$), low eddy energy level, and $\tau_{K_{E,\mathrm{BT}}}$ larger than 100 days.

Choosing $\tau_{K_{E,\mathrm{BT}}}$ as the measure for the delay time scale is based on the assumption that the dominant control factor of the variability of P_E and K_E is the energy cascade. However, bottom friction also influences the delay process in at least two ways: First, if the friction terms have a significant magnitude in the $K_{E,\mathrm{BC}}$ and $K_{E,\mathrm{BT}}$ budgets, the $P_E/K_{E,\mathrm{BC}}$ variability and thus the delay time scale are greatly influenced by both energy cascades and bottom friction. Second, baroclinic turbulence properties, such as eddy heat fluxes and how many times eddies can turn over before "feeling" the friction, are very sensitive to the "throughput," defined as $(U_1 - U_2)/(rR_d)$ (e.g., Arbic and Flierl 2004; Thompson and Young 2007). In the high throughput case, eddies will not feel bottom friction until several eddy turnover times, while in the low throughput case, variability is damped out before eddies turn over and cascade fully. For example, when U_1 is only $4\,\mathrm{km\,day^{-1}}$, the throughput is small, the eddy energy cascade process is strongly influenced by friction, and thus the star marker for the case $U_1 = 4\,\mathrm{km\,day^{-1}}$ in Fig. 14a deviates from the linear fit.

In these sensitivity experiments, as δ and $U_1 - U_2$ increase, the growth rate time scale $1/\sigma_{\max}$ decreases (not shown). Note that $1/\sigma_{\max}$ indicates how fast the initial perturbations grow, and the delay time scale represents how fast the temporal variability in one energy reservoir transfers to adjacent reservoirs. Thus, $1/\sigma_{\max}$ is not a good indicator of the delay time scale; as shown in Fig. 14b, one value of $1/\sigma_{\max}$ can correspond to more than one delay time scale.

5. Conclusions and discussion

A novel, time-dependent energy diagram for eddy–mean flow interactions (Fig. 1a) is introduced and applied to representative energetic regions in a global, eddying state estimate: the Kuroshio and Gulf Stream Extensions, a subtropical gyre patch in the North Pacific, and the Southern Ocean. This diagram is an extension of the classic Lorenz energy diagram (Lorenz 1955) to the time-dependent and nonlocal scenario. It is also an extension of the time-mean energy diagram in Chen et al. (2014a) to the time-dependent regime. It depicts the energy exchange among six energy components composing the total kinetic and available potential energy: energy in the mean flow (P_M and K_M), energy in eddies (P_E and K_E), and the energy anomaly residual (P_R and K_R).

The P_R and K_R components, not included in the classic Lorenz energy diagram, are important in the time-dependent energy diagram (Fig. 1a). They arise from the lack of scale separation between mean and eddies and have significant amplitudes compared to P_M and K_M in the selected energetic regions. The time-dependent energy diagram shows that during eddy–mean flow interactions, the mean energy reservoir (P_M and K_M) does not directly interact with the eddy energy reservoir (P_E and K_E). Instead, their interaction is through P_R and K_R. If the energy transfer rate from the mean flow to P_R and K_R is not equal to the transfer rate from P_R and K_R to eddies, eddy–mean flow interactions are nonlocal. From a time-dependent perspective, eddy and mean flow interact nonlocally in all the four regions, indicating the need to develop nonlocal eddy parameterization schemes. In future studies, P_R and K_R should be evaluated more, considering their key roles in eddy–mean flow interactions and their noticeable contribution to total energy and thus total tracer transport.

This energy diagram is a useful tool to study ocean dynamics and energetics. For example, its application to the Kuroshio and Gulf Stream Extension regions reveals the suppression phenomenon about mixed instability energetics there. Although this phenomenon has never been documented before to our knowledge, quite a few previous findings relevant to mixed instability are consistent with this phenomenon. For example, Thompson and Naveira-Garabato (2014) found that as the curvatures of meanders at topography increase (and thus the horizontal flow shear increases and barotropic instability strengthens), the baroclinicity of the flow decreases (and baroclinic instability weakens). The analogous process has also been discussed in the atmospheric and idealized scenarios (e.g., Ioannou and Lindzen 1986; Nakamura 1993; Chen et al. 2007). Further discussion is beyond the scope here.

Applying this energy diagram to the subtropical gyre and Southern Ocean regions reveals the delay phenomenon in the baroclinically unstable system. The energy transfer from P_R to P_E is coherent with the energy transfer from P_E to K_E; however, the variability of the former leads the variability of the latter. The QG model analysis indicates that this phenomenon is related to eddy–eddy interaction; it takes some time for some part of the energy transferred from $P_M + P_R$ to P_E to cascade to small-scale eddies, before being converted to K_E (Fig. 10b). The delay time is on the order of the barotropic eddy turnover time scale [Eq. (35)], which is the time scale for the energy cascade. Testing the delay mechanism proposed here in the ECCO2 model is left for future work due to space limitations.

Phenomena relevant to the delay phenomenon we identified have been reported in some previous studies (e.g., Zhang and Stone 2010). Zhang and Stone (2010) investigated the equilibration of atmospheric eddies in a multilayer, QG system with periodically varying external forcing. They found that when the forcing frequency is high (i.e., 5 cycles per year), P_E varies with P_M, but its variability lags the P_M variability by around 15–30 days. Our

investigation about the delay phenomenon is still novel in that we confirmed the existence of the delay phenomenon in realistic oceanic models, proposed a mechanism for its origin, and provided a scaling for the delay time scale.

The QG energy diagram we employed to investigate the delay phenomenon (Fig. 10b) is consistent with previous studies: 1) the forward cascade of P_E is consistent with the dual cascade scenario, which denotes the forward (inverse) cascade of the baroclinic (barotropic) mode during baroclinic turbulence (Salmon 1980); and 2) the transfer of energy from $P_M + P_R$ to P_E and then to K_E in the baroclinically unstable system is well known (Pedlosky 1987). Our contribution is that we introduced the triple decomposition energy framework, added temporal information to it, and then applied it to explain the origin of the delay.

The time-dependent, eddy-mean energy diagram introduced in this study is applicable not only to the ocean but also to other contexts of geophysical fluid dynamics (e.g., atmospheric circulation). Yet, we only carried out some preliminary application of the energy diagram. Many open questions exist. For example, the sensitivity of results presented here to the model output duration, choice of oceanic regions, and model configuration (e.g., resolution and subgrid parameterizations) are to be examined. The prevalence and origin of the delay and suppression phenomena in the ocean and atmosphere are to be further explored. Similar techniques can be used to derive the time-dependent budgets for enstrophy and tracer variance, both of which are useful quantities for studying geophysical fluid dynamics.

Acknowledgments. R. Chen thanks the support by NASA (NNX09AI87G and NNX08AR33G) and acknowledges C. Wunsch for providing insightful suggestions during the preparation of the work. A. F. Thompson is supported by NASA (NNX15AG42G), and G. R. Flierl is supported by NSF (OCE-1459702). Three anonymous reviewers provided comments, which substantially improved the work. R. X. Huang suggested the possible delay between potential and kinetic energy reservoirs. M. A. Spall provided helpful suggestions about section 4. Many thanks to J.-M. Campin, C. Hill, D. Menemenlis, and H. Zhang for discussion about the ECCO2 state estimate.

APPENDIX A

Time-Dependent Energy Equations for ECCO2 Model

a. Governing equations for kinetic energy

We start from the horizontal momentum equations from the ECCO2 state estimate:

$$\frac{\partial u_i}{\partial t} + \frac{\partial}{\partial x_j}(u_j u_i) + 2\epsilon_{ijk}\Omega_j u_k = -\frac{1}{\rho_0}\frac{\partial}{\partial x_i}p + D_i, \tag{A1}$$

where $i = 1$ and 2, denote zonal and meridional directions, and $j = 1$, 2, and 3, denote zonal, meridional, and vertical directions. Here, D_i is the friction term: $D_i = \partial/\partial z(A_z \partial u_i/\partial z) + A_4 \nabla_h^4 u_i$. The variable p is hydrostatic pressure, Ω_j is Earth's rotation vector, A_z is vertical viscosity, A_4 is horizontal biharmonic viscosity, and u_j is velocity.

A temporal average of Eq. (A1) leads to the $\overline{u}_i$ equation, where $\bar{\cdot}$ denotes the time mean. Subtracting the equation for $\overline{u}_i$ from Eq. (A1) leads to equation for u_i', where $\cdot'$ means the deviation of an variable from its time mean. Then we obtain

$$\frac{\partial}{\partial t}K_M + \frac{\partial}{\partial x_j}(\overline{u}_j K_M) + \underbrace{\rho_0 \overline{u}_i \frac{\partial}{\partial x_j}\overline{u_j' u_i'}}_{-I_{1,K_M}} = R_{K_M}, \tag{A2}$$

$$\frac{\partial}{\partial t}K_R + \frac{\partial}{\partial x_j}(u_j' K_M + \overline{u}_j K_R) + \underbrace{\rho_0 \overline{u}_i \frac{\partial}{\partial x_j} u_j' u_i' - \rho_0 \overline{u}_i \frac{\partial}{\partial x_j}\overline{u_i' u_j'} + \rho_0 u_i' \frac{\partial}{\partial x_j}\overline{u_i' u_j'}}_{-I_{1,K_R}} = R_{K_R}, \tag{A3}$$

$$\frac{\partial}{\partial t}K_E + \frac{\partial}{\partial x_j}(\overline{u}_j K_E + u_j' K_E) + \underbrace{\rho_0 u_i' u_j' \frac{\partial}{\partial x_j}\overline{u}_i - \rho_0 u_i' \frac{\partial}{\partial x_j}\overline{u_i' u_j'}}_{-I_{1,K_E}} = R_{K_E}, \quad \text{where} \tag{A4}$$

$$R_{K_M} = -\frac{\partial}{\partial x_j}(\overline{u}_j \overline{p^*}) \underbrace{-g\overline{\rho^*}\,\overline{w}}_{E_{P_M \to K_M}} + \underbrace{\rho_0 \overline{u}_i \overline{D}_i}_{X_{K_M}},$$

$$R_{K_E} = -\frac{\partial}{\partial x_j}(u_j' p') \underbrace{-g\rho' w'}_{E_{P_E \to K_E}} + \underbrace{\rho_0 u_i' D_i'}_{X_{K_E}}, \quad \text{and} \tag{A5}$$

$$R_{K_R} = -\frac{\partial}{\partial x_j}(\overline{u}_j p' + u_j' \overline{p^*}) \underbrace{-g(\overline{\rho^*} w' + \rho' \overline{w})}_{E_{P_R \to K_R}} + \underbrace{\rho_0(\overline{u}_i D_i' + u_i' \overline{D}_i)}_{X_{K_R}}, \tag{A6}$$

where $\cdot^*$ means the deviation of a variable from its global and time mean at each depth level, and w is vertical velocity. The hydrostatic assumption is used when deriving Eqs. (A2)–(A4).

Equations (A2)–(A4) is a set of time-dependent kinetic energy equations different from those employed in our diagnosis, that is, Eqs. (11)–(13). Note that I_{1,K_M} is time independent and Eq. (A2) is the same as that in the classic time-mean energy diagram (e.g., Chen et al. 2014a). However, in this equation set, the advection terms are not similar; K_M is advected by $\overline{u}_j$ only, K_E is advected by $\overline{u}_j + u_j'$, and the naturally divergent fluxes in

the K_R equation even include the advection of K_M by u_j'. Besides the asymmetry issue, another issue is that

$$I_{1,K_M} + I_{1,K_R} + I_{1,K_E} = -\frac{\partial}{\partial x_j}(u_j' K_R), \tag{A7}$$

which is generally not zero. These I_1 terms could be interpreted as the kinetic energy change due to eddy–mean flow interaction. Considering that these eddy–mean flow interaction terms involve energy exchange, not energy transformation, among reservoirs, we would expect $I_{1,K_M} + I_{1,K_R} + I_{1,K_E}$ to be zero. These issues lead to alternative derivations next.

Alternatively, considering that the total kinetic energy equation is advected by the total flow, one can choose to put all the advection terms in the K_M, K_R, and K_E equations consistently in the form of advection by the total velocity. That is, we naturally partition the advection of total kinetic energy into three components:

$$\frac{\partial}{\partial x_j}(u_j K_T) = \frac{\partial}{\partial x_j}(u_j K_M) + \frac{\partial}{\partial x_j}(u_j K_R) + \frac{\partial}{\partial x_j}(u_j K_E). \tag{A8}$$

In this case, Eqs. (A2)–(A3) can be converted to the following:

$$\frac{\partial}{\partial t}K_M + \frac{\partial}{\partial x_j}(u_j K_M) - \frac{\partial}{\partial x_j}(u_j' K_M) + \rho_0 \overline{u}_i \frac{\partial}{\partial x_j}\overline{u_j' u_i'} = R_{K_M}, \quad \text{and} \tag{A9}$$

$$\frac{\partial}{\partial t}K_R + \frac{\partial}{\partial x_j}(u_j K_R) + \frac{\partial}{\partial x_j}(u_j' K_M) - \rho_0 \frac{\partial}{\partial x_j}(u_j' u_i' \overline{u}_i) + \rho_0 \left(\overline{u}_i \frac{\partial}{\partial x_j} u_j' u_i' - \overline{u}_i \frac{\partial}{\partial x_j}\overline{u_i' u_j'} + u_i' \frac{\partial}{\partial x_j}\overline{u_i' u_j'} \right) = R_{K_R}. \tag{A10}$$

Expanding the fourth term in Eq. (A10), but keeping Eqs. (A9) and (A4) the same, gives

$$\frac{\partial}{\partial t}K_M + \frac{\partial}{\partial x_j}(u_j K_M) \underbrace{- \frac{\partial}{\partial x_j}(u_j' K_M) + \rho_0 \overline{u}_i \frac{\partial}{\partial x_j}\overline{u_j' u_i'}}_{-I_{K_M}} = R_{K_M}, \tag{A11}$$

$$\frac{\partial}{\partial t}K_R + \frac{\partial}{\partial x_j}(u_j K_R) + \underbrace{\frac{\partial}{\partial x_j}(u_j' K_M) - \rho_0 u_i' u_j' \frac{\partial}{\partial x_j}\overline{u}_i - \rho_0 \overline{u}_i \frac{\partial}{\partial x_j}\overline{u_i' u_j'} + \rho_0 u_i' \frac{\partial}{\partial x_j}\overline{u_i' u_j'}}_{-I_{K_R}} = R_{K_R}, \quad \text{and} \tag{A12}$$

$$\frac{\partial}{\partial t}K_E + \frac{\partial}{\partial x_j}(u_j K_E) + \underbrace{\rho_0 u_i' u_j' \frac{\partial}{\partial x_j}\overline{u}_i - \rho_0 u_i' \frac{\partial}{\partial x_j}\overline{u_i' u_j'}}_{-I_{K_E}} = R_{K_E}. \tag{A13}$$

Equations (A11)–(A13) are those introduced in section 2 [Eqs. (11)–(13)].

The term I_a is the change of a due to the eddy–mean flow interaction. In this case, we have

$$I_{K_M} + I_{K_R} + I_{K_E} = 0. \tag{A14}$$

Another advantage of Eqs. (A11)–(A13) is that the advection terms are symmetric. It is reasonable to consider that K_E, K_M, and K_R are all advected by the total flow.

Equations (A11) and (A12) reveal that the advection of K_M by eddy velocity $\mathbf{u}'$ is immediately and completely transferred to the K_R reservoir. The fact that the eddy advection of the K_M term appears in the K_R equation implies that the budgets of K_M and K_R are related. In fact, the third and fourth terms in Eq. (A11) are, respectively, the opposite of the third and fifth terms in Eq. (A12). The fourth and sixth terms in Eq. (A12) are the opposite of the third and fourth terms of Eq. (A13). Therefore, energy exchange can be considered to occur between K_M and K_R through I_{K_M} and between K_E and K_R through I_{K_E}. Thus, in the main text and the remaining appendix A, we denote I_{K_M} and I_{K_E} by $E_{K_R \to K_M}$ and $E_{K_R \to K_E}$, where $E_{a \to b}$ is the energy transfer from a to b.

b. *Governing equations for available potential energy*

We start from Eq. (A13) from Chen et al. (2014a), that is, the ρ^* equation:

$$\frac{\partial}{\partial t}\rho^* + \frac{\partial}{\partial x_j}(u_j \rho^*) + w n_0 = \frac{\partial}{\partial t}(\overline{\rho^*} + \rho') + \frac{\partial}{\partial x_j}[u_j(\overline{\rho^*} + \rho')] + w n_0 = H_\rho + w\widehat{\rho_z}^*, \tag{A15}$$

where ρ denotes in situ density, and n_0 is defined in Eq. (6). Here, H_ρ denotes the source/sink of ρ due to vertical mixing and air–sea exchange of heat and freshwater (Chen et al. 2014a), and $\widehat{\rho_z}$ denotes $(\partial\rho/\partial z)_{S,\theta}$. The equations for $\overline{\rho^*}$ and ρ' can be easily derived from Eq. (A15).

Following the approaches and rationale similar to those in appendix A, section a, we obtain

$$\frac{\partial}{\partial t}P_M+\frac{\partial}{\partial x_j}(u_jP_M)=\underbrace{\frac{g}{n_0}\overline{\rho^*}\frac{\partial}{\partial x_i}\overline{(u_i'\rho')}+\frac{\partial}{\partial x_i}(u_i'P_M)}_{E_{P_R\to P_M}}-\underbrace{(-g\overline{\rho^*}\,\overline{w})}_{E_{P_M\to K_M}}\underbrace{-\frac{g}{n_0}\overline{\rho^*}\,\overline{H_\rho}}_{X_{P_M}}+R_{P_M}, \tag{A16}$$

$$\frac{\partial}{\partial t}P_E+\frac{\partial}{\partial x_j}(u_jP_E)=\underbrace{\frac{g}{n_0}\rho'u_i'\frac{\partial}{\partial x_i}\overline{\rho^*}-\frac{g}{n_0}\rho'\frac{\partial}{\partial x_i}(\overline{u_i'\rho'})}_{E_{P_R\to P_E}}-\underbrace{(-g\rho'w')}_{E_{P_E\to K_E}}\underbrace{-\frac{g}{n_0}\rho'H_\rho'}_{X_{P_E}}+R_{P_E},\quad\text{and} \tag{A17}$$

$$\frac{\partial}{\partial t}P_R+\frac{\partial}{\partial x_j}(u_jP_R)=-(E_{P_R\to P_M}+E_{P_R\to P_E})-\underbrace{[-g(\overline{\rho^*}w'+\rho'\overline{w})]}_{E_{P_R\to K_R}}\underbrace{-\frac{g}{n_0}(\rho'\overline{H_\rho}+\overline{\rho^*}H_\rho')}_{X_{P_R}}+R_{P_R}, \tag{A18}$$

where i and j are defined in appendix A, section a. Here, the R terms are

$$R_{P_M}=-\frac{wP_M}{n_0}\frac{\partial n_0}{\partial z}-\frac{g\overline{\rho^*}}{n_0}\left[\overline{w\widehat{\rho_z}^*}-\frac{\partial}{\partial z}(\overline{w'\rho'})\right]+\frac{\partial}{\partial z}(w'P_M), \tag{A19}$$

$$R_{P_E}=-\frac{wP_E}{n_0}\frac{\partial n_0}{\partial z}-\frac{g\rho'}{n_0}\left[(w\widehat{\rho_z}^*)'+\frac{\partial}{\partial z}(\overline{w'\rho'})\right]+\frac{gw'\rho'}{n_0}\frac{\partial}{\partial z}\overline{\rho^*},\quad\text{and} \tag{A20}$$

$$R_{P_R}=-\frac{wP_T}{n_0}\frac{\partial n_0}{\partial z}-\frac{g\rho^*}{n_0}w\widehat{\rho_z}^*-R_{P_E}-R_{P_M}. \tag{A21}$$

c. Corresponding time-mean energy diagrams

Now consider the time mean of Eqs. (A11)–(A13). Using the property of $\overline{\overline{\cdot}}=\overline{\cdot}$, we have

$$\frac{\partial}{\partial t}K_M+\frac{\partial}{\partial x_j}(\overline{u}_jK_M)\underbrace{+\rho_0\overline{u}_i\frac{\partial}{\partial x_j}\overline{u_j'u_i'}}_{-\overline{E}_{K_R\to K_M}}=\overline{R_{K_M}}, \tag{A22}$$

$$\frac{\partial}{\partial x_j}(\overline{u_j'K_R})\underbrace{-\rho_0\overline{u_i'u_j'}\frac{\partial}{\partial x_j}\overline{u}_i-\rho_0\overline{u}_i\frac{\partial}{\partial x_j}\overline{u_i'u_j'}}_{\overline{E}_{K_R\to K_M}+\overline{E}_{K_R\to K_E}}=0, \tag{A23}$$

and

$$\frac{\partial}{\partial t}\overline{K_E}+\frac{\partial}{\partial x_j}(\overline{u_jK_E})+\underbrace{\rho_0\overline{u_i'u_j'}\frac{\partial}{\partial x_j}\overline{u}_i}_{-\overline{E}_{K_R\to K_E}}=R_{K_E}. \tag{A24}$$

Equations (A22) and (A24) are the eddy-mean kinetic energy equations often employed in previous energy studies (e.g., Kang and Curchitser 2015; Kang et al. 2016). Equations (A22) and (A24) alone do not illustrate the origin of the nonlocality of the eddy–mean flow interaction. The concept of nonlocality, introduced by Chen et al. (2014a) refers to the fact that $\overline{E}_{K_R\to K_M}+\overline{E}_{K_R\to K_E}$ does not necessarily need to be zero in a selected region.

Expanding $\overline{u_j'K_R}$ in Eq. (A23) reduces Eq. (A23) to zero, consistent with $\overline{K_R}=0$. Yet, Eq. (A23) helps clarify the nonlocality of eddy–mean flow interaction. The term $-\rho_0\overline{u}_i\partial/\partial x_j\overline{u_j'u_i'}$ is the gain or loss of K_M from K_R, while $\rho_0\overline{u_i'u_j'}\partial/\partial x_j\overline{u}_i$ is the gain or loss of K_E from K_R. Equation (A23) suggests that from a time-mean perspective, the fluxes of K_R into or out of a region through eddy advection balances the transfer to or from K_E and K_M. A similar rationale can be applied to time-mean potential energy equations.

APPENDIX B

Time-Dependent Energy Equations for QG Model

a. Governing equations of the QG two-layer model

Here are the equations for the relative vorticity in the ith layer and vertical velocity at the layer interface w:

$$\frac{\partial}{\partial t}\nabla^2\phi_i+J(-U_iy+\phi_i,\nabla^2\phi_i)+\beta\frac{\partial\phi_i}{\partial x}=(-1)^i\frac{2f_0w}{H_i}-r\delta_{i2}\nabla^2\phi_2,\quad\text{and} \tag{B1}$$

$$\frac{2f_0w}{H_1F_1}=\frac{2f_0w}{H_2F_2}=\frac{\partial}{\partial t}(\psi_2-\psi_1)+J(\psi_1,\psi_2), \tag{B2}$$

where $\psi_i=-U_iy+\phi_i$ (e.g., Vallis 2006). Compared to the layer equations, the modal equations

are more physically illuminating (Flierl 1978). The baroclinic and barotropic eddy streamfunction are, respectively, $\phi_{BC} = \sqrt{\delta}(\phi_1 - \phi_2)/(1+\delta)$ and $\phi_{BT} = (\delta\phi_1 + \phi_2)/(1+\delta)$ (Arbic 2000). Using Eq. (B1), we can easily obtain the vorticity equations in modal form:

$$\frac{\partial}{\partial t}\nabla^2\phi_{BC} + \beta\frac{\partial\phi_{BC}}{\partial x} + J(-U_{BT}y + \phi_{BT}, \nabla^2\phi_{BC}) + J(-U_{BC}y + \phi_{BC}, \nabla^2\phi_{BT}) + \frac{1-\delta}{\sqrt{\delta}}J(-U_{BC}y + \phi_{BC}, \nabla^2\phi_{BC})$$
$$= -\frac{2f_0 w\sqrt{\delta}}{H_1} + \frac{r\sqrt{\delta}}{1+\delta}\nabla^2(\phi_{BT} - \sqrt{\delta}\,\phi_{BC}), \quad \text{and} \tag{B3}$$

$$\frac{\partial}{\partial t}\nabla^2\phi_{BT} + \beta\frac{\partial\phi_{BT}}{\partial x} + J(-U_{BT}y + \phi_{BT}, \nabla^2\phi_{BT}) + J(-U_{BC}y + \phi_{BC}, \nabla^2\phi_{BC}) = -\frac{r}{1+\delta}\nabla^2(\phi_{BT} - \sqrt{\delta}\,\phi_{BC}), \tag{B4}$$

where U_{BC} and U_{BT} are, respectively, the imposed baroclinic and barotropic velocities:

$$U_{BC} = \frac{\sqrt{\delta}(U_1 - U_2)}{1+\delta}, \quad U_{BT} = \frac{\delta U_1 + U_2}{1+\delta}.$$

b. Eddy kinetic energy equations in the double decomposition framework

"Double decomposition" denotes decomposing the total flow into two parts: mean and eddies. Multiplying Eq. (B3) by $-\phi_{BC}$ and multiplying Eq. (B4) by $-\phi_{BT}$,

$$\underbrace{\frac{\partial}{\partial t}\frac{1}{2}\langle\nabla\phi_{BC}\cdot\nabla\phi_{BC}\rangle}_{\langle K_{E,BC}\rangle} = \underbrace{\left\langle\frac{2f_0}{H_2(1+\delta)}(\phi_1-\phi_2)w\right\rangle}_{\langle E_{P_E\to K_{E,BC}}\rangle} - \underbrace{\frac{r\delta}{(1+\delta)^2}\langle(\phi_1-\phi_2)\nabla^2\phi_2\rangle}_{\langle K_{E,BC_{dissi}}\rangle} - \underbrace{\langle\phi_{BT}J(-U_{BC}y+\phi_{BC},\nabla^2\phi_{BC})\rangle}_{\langle E_{K_{E,BC}\to K_{E,BT}}\rangle}, \tag{B5}$$

and

$$\underbrace{\frac{\partial}{\partial t}\frac{1}{2}\langle\nabla\phi_{BT}\cdot\nabla\phi_{BT}\rangle}_{\langle K_{E,BT}\rangle} = \underbrace{\left\langle\frac{r(\delta\phi_1+\phi_2)\nabla^2\phi_2}{(1+\delta)^2}\right\rangle}_{-\langle K_{E,BT_{dissi}}\rangle} + \underbrace{\langle\phi_{BT}J(-U_{BC}y+\phi_{BC},\nabla^2\phi_{BC})\rangle}_{\langle E_{K_{E,BC}\to K_{E,BT}}\rangle}. \tag{B6}$$

Multiplying Eq. (B2) by $F_2(\psi_2-\psi_1)/(1+\delta)$ and then domain averaging,

$$\underbrace{\frac{\partial}{\partial t}\frac{1}{2(1+\delta)}\langle F_2(\psi_1-\psi_2)^2\rangle}_{\langle P_M+P_E+P_R\rangle} = \underbrace{\left\langle\frac{2f_0}{H_2(1+\delta)}(-U_2y+U_1y)w\right\rangle}_{\langle E_{K_M+K_R\to P_M+P_R}\rangle} - \underbrace{\left\langle\frac{2f_0}{H_2(1+\delta)}(\phi_1-\phi_2)w\right\rangle}_{\langle E_{P_E\to K_{E,BC}}\rangle}. \tag{B7}$$

Multiplying Eq. (B2) by $F_2(\phi_2-\phi_1)/(1+\delta)$ and then domain averaging,

$$\underbrace{\frac{\partial}{\partial t}\frac{1}{2(1+\delta)}\langle F_2(\phi_1-\phi_2)^2\rangle}_{\langle P_E\rangle} = \underbrace{\frac{\delta(U_2-U_1)}{R_d^2(1+\delta)^2}\left\langle\phi_2\frac{\partial}{\partial x}\phi_1\right\rangle}_{\langle E_{P_M+P_R\to P_E}\rangle} - \underbrace{\left\langle\frac{2f_0}{H_2(1+\delta)}(\phi_1-\phi_2)w\right\rangle}_{\langle E_{P_E\to K_{E,BC}}\rangle}. \tag{B8}$$

Subtracting Eq. (B8) from Eq. (B7) leads to

$$\underbrace{\frac{\partial}{\partial t}\frac{1}{2(1+\delta)}\langle F_2[(\psi_1-\psi_2)^2-(\phi_1-\phi_2)^2]\rangle}_{\langle P_M+P_R\rangle} = \underbrace{\left\langle\frac{2f_0}{H_2(1+\delta)}(-U_2y+U_1y)w\right\rangle}_{\langle E_{K_M+K_R\to P_M+P_R}\rangle} - \underbrace{\frac{\delta(U_2-U_1)}{R_d^2(1+\delta)^2}\left\langle\phi_2\frac{\partial}{\partial x}\phi_1\right\rangle}_{\langle E_{P_M+P_R\to P_E}\rangle}. \tag{B9}$$

c. EAPE equations in the triple decomposition framework

Define $\cdot_L$ and $\cdot_S$ as the large-scale and small-scale components of the variable. For example, $J_S(\phi_1, \phi_2)$ is the small-scale part of $J(\phi_1, \phi_2)$. Applying a low-pass spatial filter to Eq. (B2), then multiplying it with $F_2(\phi_{2L} - \phi_{1L})/(1 + \delta)$, and domain averaging,

$$\underbrace{\frac{\partial}{\partial t}\left\langle \frac{F_2(\phi_{2L}-\phi_{1L})^2}{2(1+\delta)} \right\rangle}_{\langle P_{E,L}\rangle} = \underbrace{\left\langle \frac{F_2}{1+\delta}(\phi_{2L}-\phi_{1L})\left(-U_1\frac{\partial \phi_{2L}}{\partial x}+U_2\frac{\partial \phi_{1L}}{\partial x}\right)\right\rangle}_{\langle E_{P_M+P_R\to P_{E,L}}\rangle} - \underbrace{\left\langle \frac{2f_0}{H_2(1+\delta)} w_L(\phi_{1L}-\phi_{2L})\right\rangle}_{\langle E_{P_{E,L}\to K_{E,\mathrm{BC}}}\rangle}$$
$$- \underbrace{\left\langle \frac{F_2}{1+\delta}(\phi_{2L}-\phi_{1L})J(\phi_1,\phi_2)\right\rangle}_{\langle E_{P_{E,L}\to P_{E,S}}\rangle} + \underbrace{\left\langle \frac{F_2}{1+\delta}(\phi_{2L}-\phi_{1L})J_S(\phi_1,\phi_2)\right\rangle}_{\langle R_{P_{E,L}}\rangle}. \tag{B10}$$

Similarly, applying a high-pass spatial filter to Eq. (B2), then multiplying it with $F_2(\phi_{2S} - \phi_{1S})/(1 + \delta)$, and domain averaging lead to

$$\underbrace{\frac{\partial}{\partial t}\left\langle \frac{F_2(\phi_{2S}-\phi_{1S})^2}{2(1+\delta)} \right\rangle}_{\langle P_{E,S}\rangle} = \underbrace{\left\langle \frac{F_2}{1+\delta}(\phi_{2S}-\phi_{1S})\left(-U_1\frac{\partial \phi_{2S}}{\partial x}+U_2\frac{\partial \phi_{1S}}{\partial x}\right)\right\rangle}_{\langle E_{P_M+P_R\to P_{E,S}}\rangle} - \underbrace{\left\langle \frac{2f_0}{H_2(1+\delta)} w_S(\phi_{1S}-\phi_{2S})\right\rangle}_{\langle E_{P_{E,S}\to K_{E,\mathrm{BC}}}\rangle}$$
$$+ \underbrace{\left\langle \frac{F_2}{1+\delta}(\phi_{2L}-\phi_{1L})J(\phi_1,\phi_2)\right\rangle}_{\langle E_{P_{E,L}\to P_{E,S}}\rangle} + \underbrace{\left\langle \frac{F_2}{1+\delta}(\phi_{2S}-\phi_{1S})J_L(\phi_1,\phi_2)\right\rangle}_{\langle R_{P_{E,S}}\rangle}. \tag{B11}$$

The total EAPE P_E is not equal to the sum of $P_{E,L}$ and $P_{E,S}$. The residual P_E denotes the difference between P_E and $(P_{E,L} + P_{E,S})$:

$$\text{residual } P_E = P_E - (P_{E,L} + P_{E,S}) = \frac{F_2(\phi_{2S}-\phi_{1S})(\phi_{2L}-\phi_{1L})}{1+\delta}. \tag{B12}$$

REFERENCES

Arbic, B. K., 2000: Generation of mid-ocean eddies: the local baroclinic instability hypothesis. Ph.D. thesis, Massachusetts Institute of Technology and Woods Hole Oceanographic Institution, 290 pp.

——, and G. R. Flierl, 2004: Baroclinically unstable geostrophic turbulence in the limits of strong and weak bottom Ekman friction: application to midocean eddies. *J. Phys. Oceanogr.*, **34**, 2257–2273, doi:10.1175/1520-0485(2004)034<2257:BUGTIT>2.0.CO;2.

——, R. B. Scott, G. R. Flierl, A. J. Morten, J. G. Richman, and J. F. Shriver, 2012: Nonlinear cascades of surface oceanic geostrophic kinetic energy in the frequency domain. *J. Phys. Oceanogr.*, **42**, 1577–1600, doi:10.1175/JPO-D-11-0151.1.

——, M. Müller, J. G. Richman, J. F. Shriver, A. J. Morten, R. B. Scott, G. Sérazin, and T. Penduff, 2014: Geostrophic turbulence in the frequency–wavenumber domain: Eddy-driven low-frequency variability. *J. Phys. Oceanogr.*, **44**, 2050–2069, doi:10.1175/JPO-D-13-054.1.

Biastoch, A., and W. Krauss, 1999: The role of mesoscale eddies in the source regions of the Agulhas Current. *J. Phys. Oceanogr.*, **29**, 2303–2317, doi:10.1175/1520-0485(1999)029<2303:TROMEI>2.0.CO;2.

Bischoff, T., and A. F. Thompson, 2014: Configuration of a Southern Ocean storm track. *J. Phys. Oceanogr.*, **44**, 3072–3078, doi:10.1175/JPO-D-14-0062.1.

Brown, J. N., and A. V. Fedorov, 2010: How much energy is transferred from the winds to the thermocline on ENSO time scales? *J. Climate*, **23**, 1563–1580, doi:10.1175/2009JCLI2914.1.

Chapman, C. C., A. M. Hogg, A. E. Kiss, and S. R. Rintoul, 2015: The dynamics of Southern Ocean storm tracks. *J. Phys. Oceanogr.*, **45**, 884–903, doi:10.1175/JPO-D-14-0075.1.

Chelton, D. B., M. G. Schlax, and R. M. Samelson, 2011: Global observations of nonlinear mesoscale eddies. *Prog. Oceanogr.*, **91**, 167–216, doi:10.1016/j.pocean.2011.01.002.

Chen, G., I. M. Held, and W. A. Robinson, 2007: Sensitivity of the latitude of the surface westerlies to surface friction. *J. Atmos. Sci.*, **64**, 2899–2915, doi:10.1175/JAS3995.1.

Chen, R., G. R. Flierl, and C. Wunsch, 2014a: A description of local and nonlocal eddy–mean flow interaction in a global eddy-permitting state estimate. *J. Phys. Oceanogr.*, **44**, 2336–2352, doi:10.1175/JPO-D-14-0009.1.

——, J. L. McClean, S. T. Gille, and A. Griesel, 2014b: Isopycnal eddy diffusivities and critical layers in the Kuroshio Extension from an eddying ocean model. *J. Phys. Oceanogr.*, **44**, 2191–2211, doi:10.1175/JPO-D-13-0258.1.

——, S. T. Gille, J. L. McClean, G. R. Flierl, and A. Griesel, 2015: A multiwavenumber theory for eddy diffusivities and its application to the southeast Pacific (DIMES) region. *J. Phys. Oceanogr.*, **45**, 1877–1896, doi:10.1175/JPO-D-14-0229.1.

Davis, R. E., 1994: Diapycnal mixing in the ocean: The Osborn–Cox model. *J. Phys. Oceanogr.*, **24**, 2560–2576, doi:10.1175/1520-0485(1994)024<2560:DMITOT>2.0.CO;2.

Eden, C., L. Czeschel, and D. Olbers, 2014: Toward energetically consistent ocean models. *J. Phys. Oceanogr.*, **44**, 3160–3184, doi:10.1175/JPO-D-13-0260.1.

Emery, W. J., and R. E. Thomson, 2004: *Data Analysis Methods in Physical Oceanography*. Elsevier, 638 pp.

Ferrari, R., and K. L. Polzin, 2005: Finescale structure of the *T–S* relation in the eastern North Atlantic. *J. Phys. Oceanogr.*, **35**, 1437–1454, doi:10.1175/JPO2763.1.

——, and C. Wunsch, 2009: Ocean circulation kinetic energy—reservoirs, sources and sinks. *Annu. Rev. Fluid Mech.*, **41**, 253–282, doi:10.1146/annurev.fluid.40.111406.102139.

Flierl, G. R., 1978: Models of vertical structure and the calibration of two-layer models. *Dyn. Atmos. Oceans*, **2**, 341–381, doi:10.1016/0377-0265(78)90002-7.

Gnanadesikan, A., M.-A. Pradal, and R. Abernathey, 2015: Isopycnal mixing by mesoscale eddies significantly impacts oceanic anthropogenic carbon uptake. *Geophys. Res. Lett.*, **42**, 4249–4255, doi:10.1002/2015GL064100.

Gregory, J. M., 2000: Vertical heat transports in the ocean and their effect on time-dependent climate change. *Climate Dyn.*, **16**, 501–515, doi:10.1007/s003820000059.

Hogg, A. M., M. P. Meredith, D. P. Chambers, E. P. Abrahamsen, C. W. Hughes, and A. K. Morrison, 2015: Recent trends in the Southern Ocean eddy field. *J. Geophys. Res. Oceans*, **120**, 257–267, doi:10.1002/2014JC010470.

Huang, R. X., 2010: *Ocean Circulation: Wind-Driven and Thermohaline Processes*. Cambridge University Press, 806 pp.

——, W. Wang, and L. L. Liu, 2006: Decadal variability of wind-energy input to the World Ocean. *Deep-Sea Res. II*, **53**, 31–41, doi:10.1016/j.dsr2.2005.11.001.

Ioannou, P., and R. S. Lindzen, 1986: Baroclinic instability in the presence of barotropic jets. *J. Atmos. Sci.*, **43**, 2999–3014, doi:10.1175/1520-0469(1986)043<2999:BIITPO>2.0.CO;2.

Johnson, T. J., R. H. Stewart, C. K. Shum, and B. D. Tapley, 1992: Distribution of Reynolds stress carried by mesoscale variability in the Antarctic Circumpolar Current. *Geophys. Res. Lett.*, **19**, 1201–1204, doi:10.1029/92GL01287.

Kang, D., and E. N. Curchitser, 2015: Energetics of eddy–mean flow interactions in the Gulf Stream region. *J. Phys. Oceanogr.*, **45**, 1103–1120, doi:10.1175/JPO-D-14-0200.1.

——, ——, and A. Rosati, 2016: Seasonal variability of the Gulf Stream kinetic energy. *J. Phys. Oceanogr.*, **46**, 1189–1207, doi:10.1175/JPO-D-15-0235.1.

Killworth, P. D., 1997: On the parameterization of eddy transfer. Part I: Theory. *J. Mar. Res.*, **55**, 1171–1197, doi:10.1357/0022240973224102.

Kontoyiannis, H., 1997: Quasi-geostrophic modeling of mixed instabilities in the Gulf Stream near 73°W. *Dyn. Atmos. Oceans*, **26**, 133–158, doi:10.1016/S0377-0265(96)00488-5.

Liang, J.-H., J. C. McWilliams, J. Kurian, F. Colas, P. Wang, and Y. Uchiyama, 2012: Mesoscale variability in the northeastern tropical Pacific: Forcing mechanisms and eddy properties. *J. Geophys. Res.*, **117**, C07003, doi:10.1029/2012JC008008.

Lorenz, E. N., 1955: Available potential energy and the maintenance of the general circulation. *Tellus*, **7A**, 157–167, doi:10.1111/j.2153-3490.1955.tb01148.x.

Marchesiello, P., J. McWilliams, and A. Shchepetkin, 2003: Equilibrium structure and dynamics of the California Current System. *J. Phys. Oceanogr.*, **33**, 753–783, doi:10.1175/1520-0485(2003)33<753:ESADOT>2.0.CO;2.

Mata, M., S. Wijffels, J. Church, and M. Tomczak, 2006: Eddy shedding and energy conversions in the East Australian Current. *J. Geophys. Res.*, **111**, C09034, doi:10.1029/2006JC003592.

Menemenlis, D., J. Campin, P. Heimbach, C. Hill, T. Lee, A. Nguyen, M. Schodlock, and H. Zhang, 2008: ECCO2: High resolution global ocean and sea ice data synthesis. Mercator Ocean Quarterly Newsletter, No. 31, Mercator Ocean, Ramonville Saint-Agne, France, 13–21.

Meredith, M. P., and A. M. Hogg, 2006: Circumpolar response of Southern Ocean eddy activity to a change in the southern annular mode. *Geophys. Res. Lett.*, **33**, L16608, doi:10.1029/2006GL026499.

Murakami, S., 2011: Atmospheric local energetics and energy interactions between mean and eddy fields. Part I: Theory. *J. Atmos. Sci.*, **68**, 760–768, doi:10.1175/2010JAS3664.1.

——, R. Ohgaito, and A. Abe-Ouchi, 2011: Atmospheric local energetics and energy interactions between mean and eddy fields. Part II: An example for the Last Glacial Maximum climate. *J. Atmos. Sci.*, **68**, 533–552, doi:10.1175/2010JAS3583.1.

Nakamura, N., 1993: An illustrative model of instabilities in meridionally and vertically sheared flows. *J. Atmos. Sci.*, **50**, 357–376, doi:10.1175/1520-0469(1993)050<0357:AIMOII>2.0.CO;2.

Oort, A. H., and J. P. Peixóto, 1983: Global angular momentum and energy balance requirements from observations. *Advances in Geophysics*, Vol. 25, Academic Press, 355–490, doi:10.1016/S0065-2687(08)60177-6.

——, S. Ascher, S. Levitus, and J. Peixóto, 1989: New estimates of the available potential energy in the world ocean. *J. Geophys. Res.*, **94**, 3187–3200, doi:10.1029/JC094iC03p03187.

——, L. Anderson, and J. Peixóto, 1994: Estimates of the energy cycle of the oceans. *J. Geophys. Res.*, **99**, 7665–7688, doi:10.1029/93JC03556.

Panetta, R. L., 1993: Zonal jets in wide baroclinically unstable regions: persistence and scale selection. *J. Atmos. Sci.*, **50**, 2073–2106, doi:10.1175/1520-0469(1993)050<2073:ZJIWBU>2.0.CO;2.

Pedlosky, J., 1987: *Geophysical Fluid Dynamics.* Springer-Verlag, 710 pp.

Phillips, N. A., 1954: Energy transformations and meridional circulations associated with simple baroclinic waves in a two-level, quasi-geostrophic model. *Tellus*, **6A**, 273–286, doi:10.1111/j.2153-3490.1954.tb01123.x.

Qiu, B., and S. Chen, 2004: Seasonal modulations in the eddy field of the South Pacific Ocean. *J. Phys. Oceanogr.*, **34**, 1515–1527, doi:10.1175/1520-0485(2004)034<1515:SMITEF>2.0.CO;2.

——, and ——, 2010: Eddy-mean flow interaction in the decadally modulating Kuroshio Extension system. *Deep-Sea Res. II*, **57**, 1098–1110, doi:10.1016/j.dsr2.2008.11.036.

Salmon, R., 1980: Baroclinic instability and geostrophic turbulence. *Geophys. Astrophys. Fluid Dyn.*, **15**, 167–211, doi:10.1080/03091928008241178.

Scott, R. B., and F. Wang, 2005: Direct evidence of an oceanic inverse kinetic energy cascade from satellite altimetry. *J. Phys. Oceanogr.*, **35**, 1650–1666, doi:10.1175/JPO2771.1.

——, and B. K. Arbic, 2007: Spectral energy fluxes in geostrophic turbulence: Implications for ocean energetics. *J. Phys. Oceanogr.*, **37**, 673–688, doi:10.1175/JPO3027.1.

——, and Y. Xu, 2009: An update on the wind power input to the surface geostrophic flow of the world ocean. *Deep-Sea Res. I*, **56**, 295–304, doi:10.1016/j.dsr.2008.09.010.

Spence, P., O. A. Saenko, M. Ebay, and A. J. Weaver, 2009: The Southern Ocean overturning: Parameterized versus permitted eddies. *J. Phys. Oceanogr.*, **39**, 1634–1651, doi:10.1175/2009JPO4120.1.

Stammer, D., and C. Wunsch, 1999: Temporal changes in eddy energy of the oceans. *Deep-Sea Res. II*, **46**, 77–108, doi:10.1016/S0967-0645(98)00106-4.

Thompson, A. F., 2010: Jet formation and evolution in baroclinic turbulence with simple topography. *J. Phys. Oceanogr.*, **40**, 257–278, doi:10.1175/2009JPO4218.1.

——, and W. R. Young, 2006: Scaling baroclinic eddy fluxes: Vortices and energy balance. *J. Phys. Oceanogr.*, **36**, 720–738, doi:10.1175/JPO2874.1.

——, and ——, 2007: Two-layer baroclinic eddy heat fluxes: Zonal flows and energy balance. *J. Atmos. Sci.*, **64**, 3214–3231, doi:10.1175/JAS4000.1.

——, and A. C. Naveira-Garabato, 2014: Equilibration of the Antarctic Circumpolar Current by standing meanders. *J. Phys. Oceanogr.*, **44**, 1811–1828, doi:10.1175/JPO-D-13-0163.1.

Tulloch, R., J. Marshall, C. Hill, and K. S. Smith, 2011: Scales, growth rates, and spectral fluxes of baroclinic instability in the ocean. *J. Phys. Oceanogr.*, **41**, 1057–1076, doi:10.1175/2011JPO4404.1.

Vallis, G. K., 2006: *Atmospheric and Oceanic Fluid Dynamics*. Cambridge University Press, 745 pp.

Venaille, A., G. K. Vallis, and K. S. Smith, 2011: Baroclinic turbulence in the ocean: analysis with primitive equation and quasigeostrophic simulations. *J. Phys. Oceanogr.*, **41**, 1605–1623, doi:10.1175/JPO-D-10-05021.1.

von Storch, J. S., C. Eden, I. Fast, H. Haak, D. Hernández-Deckers, E. Maier-Reimer, J. Marotzke, and D. Stammer, 2012: An estimate of the Lorenz energy cycle for the world ocean based on the 1/10° STORM/NCEP simulation. *J. Phys. Oceanogr.*, **42**, 2185–2205, doi:10.1175/JPO-D-12-079.1.

Waterman, S. N., and S. R. Jayne, 2011: Eddy-mean flow interactions in the along-stream development of a western boundary current jet: An idealized model study. *J. Phys. Oceanogr.*, **41**, 682–707, doi:10.1175/2010JPO4477.1.

Williams, R. G., C. Wilson, and C. W. Hughes, 2007: Ocean and atmosphere storm tracks: The role of eddy vorticity forcing. *J. Phys. Oceanogr.*, **37**, 2267–2289, doi:10.1175/JPO3120.1.

Winters, K. B., P. N. Lombard, J. J. Riley, and E. A. D'Asaro, 1995: Available potential energy and mixing in density-stratified fluids. *J. Fluid Mech.*, **289**, 115–128, doi:10.1017/S002211209500125X.

Wunsch, C., 1998: The work done by the wind on the oceanic general circulation. *J. Phys. Oceanogr.*, **28**, 2332–2340, doi:10.1175/1520-0485(1998)028<2332:TWDBTW>2.0.CO;2.

——, 2015: *Modern Observational Physical Oceanography: Understanding the Global Ocean*. Princeton University Press, 493 pp.

——, and R. Ferrari, 2004: Vertical mixing, energy, and the general circulation of the oceans. *Annu. Rev. Fluid Mech.*, **36**, 281–314, doi:10.1146/annurev.fluid.36.050802.122121.

Zemskova, V. E., B. L. White, and A. Scotti, 2015: Available potential energy and the general circulation: Partitioning wind, buoyancy forcing, and diapycnal mixing. *J. Phys. Oceanogr.*, **45**, 1510–1531, doi:10.1175/JPO-D-14-0043.1.

Zhai, X., H. L. Johnson, D. P. Marshall, and C. Wunsch, 2012: On the wind power input to the ocean general circulation. *J. Phys. Oceanogr.*, **42**, 1357–1365, doi:10.1175/JPO-D-12-09.1.

Zhang, Y., and P. H. Stone, 2010: Baroclinic eddy equilibration under specified seasonal forcing. *J. Atmos. Sci.*, **67**, 2632–2648, doi:10.1175/2010JAS3392.1.